The Design and Demonstration of Monocrystalline CdTe/MgCdTe Double-Heterostructure Solar Cells

by

Yuan Zhao

A Dissertation Presented in Partial Fulfillment
of the Requirements for the Degree
Doctor of Philosophy

Approved November 2016 by the
Graduate Supervisory Committee:

Yong-Hang Zhang, Chair
Mariana Bertoni
Richard King
Zachary Holman

ARIZONA STATE UNIVERSITY

December 2016

ABSTRACT

Cadmium Telluride (CdTe) possesses preferable optical properties for photovoltaic (PV) applications: a near optimum bandgap of 1.5 eV, and a high absorption coefficient of over 15,000 cm^{-1} at the band edge. The detailed-balance limiting efficiency is 32.1% with an open-circuit voltage (V_{oc}) of 1.23 V under the AM1.5G spectrum. The record polycrystalline CdTe thin-film cell efficiency has reached 22.1%, with excellent short-circuit current densities (J_{sc}) and fill-factors (FF). However, the V_{oc} (~900 mV) is still far below the theoretical value, due to the large non-radiative recombination in the polycrystalline CdTe absorber, and the low-level p-type doping.

Monocrystalline CdTe/MgCdTe double-heterostructures (DHs) grown on lattice-matched InSb substrates have demonstrated impressively long carrier lifetimes in both unintentionally doped and Indium-doped n-type CdTe samples. The non-radiative recombination inside of, and at the interfaces of the CdTe absorbers in CdTe/MgCdTe DH samples has been significantly reduced due to the use of lattice-matched InSb substrates, and the excellent passivation provided by the MgCdTe barrier layers. The external luminescent quantum efficiency (η_{ext}) of n-type CdTe/MgCdTe DHs is up to 3.1%, observed from a 1-μm-thick CdTe/MgCdTe DH doped at 10^{17} cm^{-3}. The 3.1% η_{ext} corresponds to an internal luminescent quantum efficiency (η_{int}) of 91%. Such a high η_{ext} gives an implied V_{oc}, or quasi-Fermi-level splitting, of 1.13 V.

To obtain actual V_{oc}, the quasi-Fermi-level splitting should be extracted to outside the circuit using a hole-selective contact layer. However, CdTe is difficult to be doped p-type, making it challenging to make efficient PN junction CdTe solar cells. With the use of MgCdTe barrier layers, the hole-contact layer can be defective without affecting the

voltage. P-type hydrogenated amorphous silicon is an effective hole-selective contact for CdTe solar cells, enabling monocrystalline CdTe/MgCdTe DH solar cells to achieve V_{oc} over 1.1 V, and a maximum active area efficiency of 18.8% (J_{sc} = 23.3 mA/cm^2, V_{oc} = 1.114 V, and FF = 72.3%). The knowledge gained through making the record-efficiency monocrystalline CdTe cell, particularly the n-type doping and the double-heterostructure design, may be transferable to polycrystalline CdTe thin-film cells and improve their competitiveness in the PV industry.

ACKNOWLEDGMENTS

The making of record-efficient monocrystalline CdTe/MgCdTe double heterostructure solar cells is built upon years of hard work by the MBE optoelectronic group led by Dr. Yong-Hang Zhang. I am grateful to many current and previous group members, to name a few, Dr. Yong-Hang Zhang, Dr. Jiang-Bo Wang, Dr. Ding Ding, Dr. Weiquan Yang, Dr. Michael DiNezza, Dr. Shi Liu, Xin-Hao Zhao, Jacob Becker, Ying-Shen Kuo, Calli Campbell, Max Lassise, Dr. Ernesto Suarez, Cheng-Ying Tsai, Zhi-Yuan Lin, Zhao-Yu He, et al.

The research would be impossible without the collaborative environment at Arizona State University. I would like to thank Dr. Mathieu Boccard, and Dr. Zachary Holman for their help on device processing and input of knowledge.

I would also like to thank the other members of my committee, Dr. Richard King and Dr. Mariana Bertoni, for their advice and interest in my research.

Finally, I am grateful to my parents for their love and support throughout the study.

TABLE OF CONTENTS

Page

CHAPTER Page

LIST OF TABLES

Table Page

LIST OF FIGURES

Figure Page

Figure Page

Figure Page

CHAPTER 1
INTRODUCTION

1.1 Why Solar?

Almost all kinds of energy people use ultimately come from the sun, including wind, hydro, biomass, and fossil fuel. Fossil fuel is the solar energy captured through photosynthesis by ancient plants. The use of fossil fuel (particularly coal) triggered the Industrial Revolution in Britain in 1700s, and significantly pushed forward the advancement of human civilization. However, this came with a price. The burning of fossil fuel releases carbon dioxide, a greenhouse gas, and many other pollutants into the atmosphere.

Solar energy is renewable, abundant, and ubiquitous. The solar cell is an optoelectronic device that directly converts sunlight to electricity through the photovoltaic (PV) effect. The cost of electricity generated by PV systems is low enough to compete with electricity generated by burns fossil fuel in many sunny areas around the world [1][2]. There are lots of interesting physics, material science, and thermodynamics in solar cells. This dissertation aims to summarize or answer some basic questions about solar cells, including

(1) What is the limiting efficiency of solar cells?

(2) What is an ideal photovoltaic absorber?

(3) What is an ideal solar cell structure?

(4) An experimental demonstration of an efficient CdTe solar cell.

1.2 The Detailed-Balance Limit of Solar Cells

The Shockley- Queisser's detailed-balance model studies the limiting efficiency of single-junction solar cells [3]. In the model, the absorptance and emittance spectra of a solar cell are zero below, and unity above the bandgap. At open-circuit, the luminescence from the cell balances the incident photons from the sunlight as illustrated in Fig. 1-1.

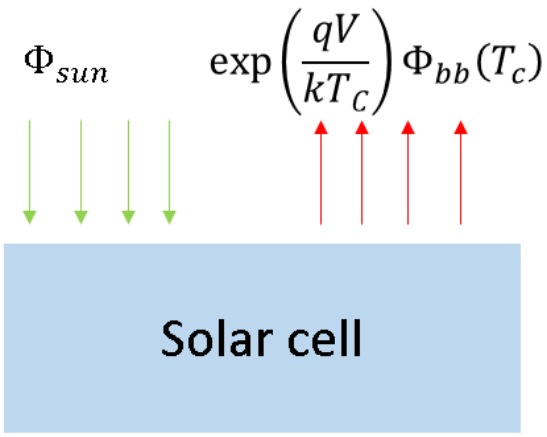

Fig. 1-1 A Solar Cell Working at the Detailed-Balance Limit.

Without any reflection losses, the short-circuit current density J_{sc} of a solar cell is determined by the number of photons above the absorber bandgap:

$$J_{sc} = q\int_{E_g}^{\infty}\Phi_{sun}(E)\,\mathrm{d}E \tag{1.1}$$

where E is the photon energy; Φ_{sun} is the photon flux density of solar radiation, which is approximated as a diluted black-body radiation source at a temperature of T_s=6000 K:

$$\Phi_{sun}(E) = f_{\omega} \frac{2\pi E^2}{h^3 c^2} \frac{1}{e^{\frac{E}{kT_c}} - 1} \tag{1.2}$$

where f_{ω} is the dilution factor:

$$f_{\omega} = \left(\frac{D}{2L}\right)^2 \tag{1.3}$$

where $D = 1.392 \times 10^6$ km is the diameter of the sun, and $L = 1.496 \times 10^8$ km is the distance from the sun to the earth.

The radiative recombination current density in a solar cell is related to the forward-bias voltage V through:

$$J_{Rad}(V) = J_0 \left[\exp\left(\frac{qV}{kT_C}\right) - 1\right] \tag{1.4}$$

where J_0 is the dark current density determined by the thermal radiation at equilibrium, and is expressed as:

$$J_0 = q \int_{E_g}^{\infty} \Phi_{bb}(T_c, E) \mathrm{d}E \tag{1.5}$$

where T_c is the temperature of the solar cell, assumed to be 300 K, unless stated otherwise; $\Phi_{bb}(T_c, E)$ is the photon flux density of a black-body (# of photons per unit area, per unit energy interval, per time).

$$\Phi_{bb}(T_c, E) = \frac{2\pi E^2}{h^3 c^2} \frac{1}{e^{\frac{E}{kT_c}} - 1} \tag{1.6}$$

In summary, the detailed-balance model gives the maximum J_{sc}, and the minimum J_0 of an ideal single-junction solar cell. As a result, the I-V curve under the detailed-balance limit is obtained. The limiting efficiency is the maximum power point on the I-V curve.

1.3 Organization of the Dissertation

The Shockley and Queisser's model assumes that the solar cell is thick enough to absorb all photons above the bandgap of absorber, without considering the thickness of solar cells. Some questions remain to be answered.

First, what is the efficiency of a solar cell with finite thickness? Chapter 2 developes a detailed-balance model for solar cells with finite thickness. Only a small fraction of luminescence escapes out of the front surface of a solar cell. The remainder of luminescent photons may be reabsorbed and reemitted, a phenomenon known as photon recycling. Chapter 2 develops a method to calculate the photon-recycling factor.

Second, what is the limiting efficiency of a solar cell with a non-step like absorptance spectrum? Is it possible to exceed the Shockley and Queisser limit? Chapter 3 answers this question.

Third, what is an ideal photovoltaic material? An ideal photovoltaic material should have unity electron-to-photon conversion efficiency, i.e. unity internal luminescence quantum efficiency. Chapter 4 studied the internal and external luminescence quantum efficiency of monocrystalline CdTe/MgCdTe double-heterostructures.

Fourth, what is an ideal solar cell structure? An ideal solar cell structure is a high quality photovoltaic absorber sandwiched between carrier-selective electron and hole contacts. Chapter 5 describes an experimental demonstration of monocrystalline CdTe with p-type amorphous silicon as the hole-selective contact. A record high open-circuit voltage of over 1.1 V has been achieved in the solar cell.

CHAPTER 2
SOLAR CELL THEORIES: FROM DETAILED-BALANCE MODEL TO EXTERNAL LUMINESCENCE QUANTUM EFFICIENCY

2.1 Introduction

In the Shockley-Queisser model [3], the absorptance spectrum of a solar cell is a Heaviside step-function centered at the bandgap energy, i.e. zero below and unity above the bandgap. To achieve this condition, the solar cell should be optically thick. Thicker absorber comes with more non-radiative recombination centers, increased material-consumption, and lower carrier-collection efficiency. Solar cell efficiencies can be improved by reducing the physical thicknesses while employing light trapping techniques to boost the absorptance [4][5].

In this chapter, detailed-balance model of solar cells with arbitrary absorber thickness is developed. The absorptance of solar cells is calculated using ray-optics approach and the detailed-balance limit of these cells (whether optically thin or optically thick) can be obtained. As pointed out in [6], the detailed-balance model takes into account the photon recycling (PR) effect. In addition, in this paper, the PR factor (the average probability for a photon-generated in a solar cell to get reabsorbed [7]) can be calculated from the detailed-balance model.

2.2 Detailed-Balance Model of Solar Cells

Consider a flat solar cell facing toward the sun, as shown in Fig. 2-1 and Fig. 2-2. Assuming the carrier collection efficiency is unity, the short circuit current density J_{sc} for a solar cell is [4]:

$$J_{sc} = q \int_0^{\infty} \mathrm{d}E \int_{\Omega} A_{\Omega,\mathrm{E}} \phi_{sun}(E, \Omega) \mathrm{d}\Omega \tag{2.1}$$

where E is photon energy; Ω is solid angle; $A_{\Omega,\mathrm{E}}$ is spectral directional spectral absorptance, defined as the percentage of light absorbed at a specific energy and direction; $\phi_{sun}(E, \Omega)$ is the spectral directional photon flux density of solar radiation, the photon flux per unit time, area, energy interval, and solid angle. The unit is #/s/cm^2/eV/sr.

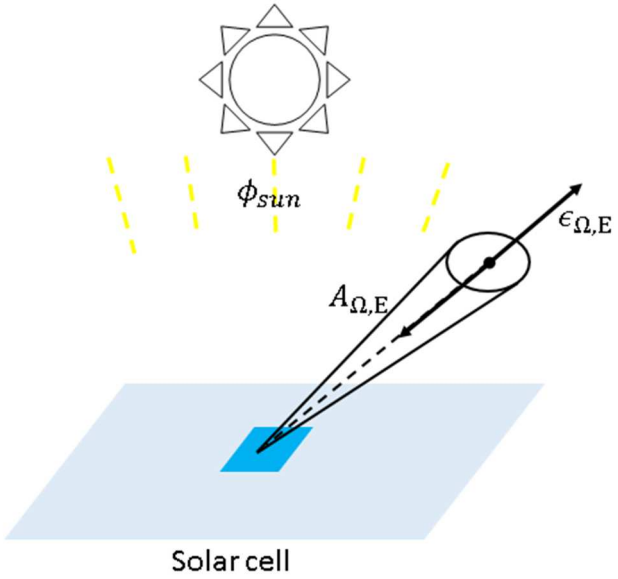

Fig. 2-1 Spectral Directional Absorptance and Emittance of a Solar Cell.

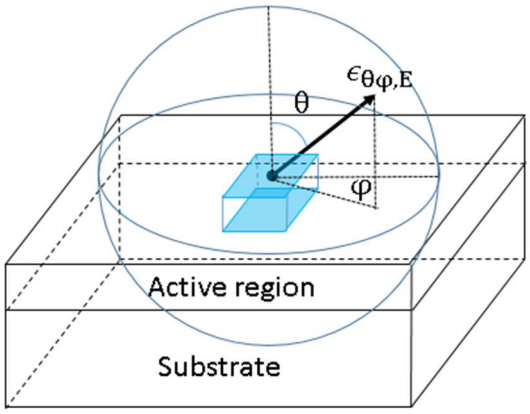

Fig. 2-2 The Parameterization of Spectral Directional Emittance

Assuming that only the unavoidable radiative recombination exists in the solar cell, the recombination current density is related to the forward-bias voltage V through the function:

$$J_{Rad} = J_0 \left[\exp\left(\frac{qV}{kT}\right) - 1 \right] \tag{2.2}$$

where J_0 is the dark current density determined by the thermal radiation at equilibrium:

$$J_0 = q \int_0^\infty \mathrm{d}E \int_\Omega \epsilon_{\Omega,\mathrm{E}} \phi_{bb}(T, E, \Omega) \mathrm{d}\Omega \tag{2.3}$$

where T is the temperature of the solar cell, usually assumed to be 300 K. $\epsilon_{\Omega,\mathrm{E}}$ is the spectral directional emittance, the ratio of emitted photon flux density to that of a black-body. $\phi_{bb}(T, E, \Omega)$ is the spectral directional photon flux density of black-body radiation at temperature T per unit time, area, energy interval, and solid angle (#/s/cm^2/eV/sr). It is expressed in Planck's law:

$$\phi_{bb}(T, E, \Omega) = \frac{2E^2}{h^3 c^2} \frac{1}{e^{\frac{E}{kT}} - 1} \tag{2.4}$$

According to Kirchhoff's law of thermal radiation, the spectral directional emittance equals absorptance:

$$A_{\Omega,\mathrm{E}} = \epsilon_{\Omega,\mathrm{E}} \tag{2.5}$$

To simplify the expression of J_{sc} in Eq. (2.1), the direction of solar radiation is assumed to be normal to the solar cell. So, J_{sc} is simplified as:

$$J_{sc} = q \int_0^{\infty} A_{\mathrm{E}} \Phi_{sun}(E)\, \mathrm{d}E \tag{2.6}$$

where A_{E} is the absorptance of solar cell at normal direction; and Φ_{sun} is the spectral photon flux density, the photon flux per unit time, energy interval, and area. The unit is #/s/cm^2/eV.

J_{sc} can be expressed in terms of the effective absorptance $\overline{A_{\mathrm{E}}}$ as:

$$J_{sc} = q\overline{A_{\mathrm{E}}} \int_{E_g}^{\infty} \Phi_{sun}(E)\, \mathrm{d}E \tag{2.7}$$

The effective absorptance $\overline{A_{\mathrm{E}}}$ characterizes the average absorptance of solar cell over the absorption spectrum and is defined as:

$$\overline{A_{\mathrm{E}}} = \frac{\int_0^{\infty} A_{\mathrm{E}} \Phi_{sun}(E)\, \mathrm{d}E}{\int_{E_g}^{\infty} \Phi_{sun}(E)\, \mathrm{d}E} \tag{2.8}$$

In spherical coordinate, the spectral directional emittance is parameterized by the zenith and azimuth angles, or $\epsilon_{\theta\varphi,\mathrm{E}}$, as shown in Fig. 2-2. The dark current density is:

$$
\begin{aligned}
&J_0 \\
&= q\int_0^{\infty} \mathrm{d}E \int_0^{2\pi} \mathrm{d}\varphi \int_0^{\frac{\pi}{2}} \sin\theta\, \epsilon_{\theta\varphi,\mathrm{E}} \phi_{bb,air}(T,E,\theta,\varphi)\mathrm{d}\theta \\
&+\ q\int_0^{\infty} \mathrm{d}E \int_0^{2\pi} \mathrm{d}\varphi \int_{\frac{\pi}{2}}^{\pi} -\sin\theta\, \epsilon_{\theta\varphi,\mathrm{E}} \phi_{bb,sub}(T,E,\theta,\varphi)\mathrm{d}\theta
\end{aligned}
\tag{2.9}
$$

where $\phi_{bb,air}(T,E,\theta,\varphi)$ and $\phi_{bb,sub}(T,E,\theta,\varphi)$ are the spectral directional photon flux density of black-body radiation in the air and in the substrate, respectively. According to Planck's law and Lambert's cosine law, the expressions are:

$$
\phi_{bb,air}(T,E,\theta,\varphi) = \cos\theta \frac{2E^2}{h^3c^2} \frac{1}{e^{\frac{E}{kT}} - 1} \tag{2.10}
$$

$$
\phi_{bb,sub}(T,E,\theta,\varphi) = \cos\theta \frac{2E^2 n_r^2}{h^3c^2} \frac{1}{e^{\frac{E}{kT}} - 1} \tag{2.11}
$$

It is worth noting that the black-body radiation in the substrate (with refractive index of n_r) is n_r^2 times that of black-body radiation in the air, due to the increased photon density of states in the substrate. Spectral directional emittance is usually independent of the azimuth angle φ, and thus can be simply written as $\epsilon_{\theta,\mathrm{E}}$. Therefore, the dark current density of a solar cell structure is:

$$
\begin{aligned}
&J_0 \\
&= q\int_0^{\infty} \frac{2\pi E^2}{h^3c^2} \frac{1}{e^{\frac{E}{kT}} - 1} \mathrm{d}E \int_0^{\frac{\pi}{2}} 2\sin\theta\cos\theta\, \epsilon_{\theta,\mathrm{E}} \mathrm{d}\theta \\
&+\ q\int_0^{\infty} \frac{2\pi E^2 n_r^2}{h^3c^2} \frac{1}{e^{\frac{E}{kT}} - 1} \mathrm{d}E \int_{\frac{\pi}{2}}^{\pi} -2\sin\theta\cos\theta\, \epsilon_{\theta,\mathrm{E}} \mathrm{d}\theta
\end{aligned}
\tag{2.12}
$$

We define emittance of front surface ϵ_E^f and emittance of back surface ϵ_E^b as

$$\epsilon_E^f = \int_0^{\frac{\pi}{2}} 2\sin\theta\cos\theta\,\epsilon_{\theta,\mathrm{E}}\mathrm{d}\theta \tag{2.13}$$

$$\epsilon_E^b = \int_{\frac{\pi}{2}}^{\pi} -2\sin\theta\cos\theta\,\epsilon_{\theta,\mathrm{E}}\mathrm{d}\theta \tag{2.14}$$

Using the surface emittance, dark current density is:

$$J_0 = q\int_0^{\infty}\left(\epsilon_E^f + n_r^2\epsilon_E^b\right)\Phi_{bb}(T,E)\mathrm{d}E \tag{2.15}$$

where $\Phi_{bb}(T,E) = \frac{2\pi E^2}{h^3c^2}\frac{1}{e^{\frac{E}{kT}}-1}$ is spectral photon flux density of black-body radiation of a flat surface facing free space, in the unit of #/s/cm^2/eV.

Similar to the expression of J_{sc}, dark current density can be expressed in terms of effective emittances:

$$J_0 = q\left(\overline{\epsilon_E^f} + n_g^2\overline{\epsilon_E^b}\right)\int_{E_g}^{\infty}\Phi_{bb}(T,E)\mathrm{d}E \tag{2.16}$$

where n_g is the average refractive index around the bandgap (refractive index can be moved out of the integral because spontaneous emission is concentrated near the bandgap and refractive index is a slowly varying parameter at that small range); $\overline{\epsilon_E^f}$ and $\overline{\epsilon_E^b}$ are effective emittances of front (toward the sun) and back (opposite to the sun) surfaces, defined as

$$\overline{\epsilon_E^f} = \frac{\int_0^{\infty}\epsilon_E^f\frac{2\pi E^2}{h^3c^2}\frac{1}{e^{\frac{E}{kT}}-1}\mathrm{d}E}{\int_{E_g}^{\infty}\frac{2\pi E^2}{h^3c^2}\frac{1}{e^{\frac{E}{kT}}-1}\mathrm{d}E} \tag{2.17}$$

$$\overline{\epsilon_E^b} = \frac{\int_0^\infty n_r^2 \epsilon_E^b \frac{2\pi E^2}{h^3 c^2} \frac{1}{e^{\frac{E}{kT}} - 1} \mathrm{d}E}{n_g^2 \int_{E_g}^\infty \frac{2\pi E^2}{h^3 c^2} \frac{1}{e^{\frac{E}{kT}} - 1} \mathrm{d}E} \tag{2.18}$$

In summary, given a solar cell, the emittance/absorptance to every direction as a function of photon energy should be known first. Then, integrate the spectral directional absorptance $A_{\Omega,\mathrm{E}}$ times the photon flux density of solar radiation $\phi_{sun}(E, \Omega)$ to calculate the short-circuit current density, J_{sc}. Next, integrate the spectral directional emittance times the photon flux density $\epsilon_{\Omega,\mathrm{E}}$ of the black-body radiation at room temperature to calculate the dark current density J_0. As a result, the I-V curve under the detailed-balance limit is obtained. The limiting efficiency can be calculated using the maximum power point on the I-V curve.

2.3 Photon Recycling and Photon Extraction Factors

Photon generated through radiative recombination in solar cell has four possible destinies [7]:

1. Emit from the top surface, with probability γ_e^f;

2. Emit to substrate, with probability γ_e^b;

3. Get absorbed in the absorber region incurring band-to-band transition, with probability γ_r;

4. Get absorbed parasitically without incurring band-to-band transition, with probability γ_l.

The four possibilities sum up to one:

$$\gamma_e^f + \gamma_e^b + \gamma_r + \gamma_l = 1 \tag{2.19}$$

The third process is photon recycling (PR), and γ_r is referred as PR factor. If radiative recombination is uniform within the solar cell, PR effect results in a reduced net radiative recombination rate according to:

$$R_{rad} = B_0(1 - \gamma_r)np \tag{2.20}$$

where n and p are the electron and hole concentration, respectively; B_0 is the material's intrinsic radiative recombination coefficient, a parameter independent of the sample geometry.

PR effect is equivalent to lowering the effective radiative recombination coefficient B_{eff}:

$$B_{eff} = B_0(1 - \gamma_r) \tag{2.21}$$

Since the PR effect is dependent on solar cell structure properties such as thickness and surface roughness, B_{eff} is specific to a solar cell structure as well.

At equilibrium, the rate of photon flux density emitting from the front surface is:

$$R_{rad}^f = \overline{\epsilon_E^f} \int_{E_g}^{\infty} \frac{2\pi E^2}{h^3 c^2} \frac{1}{e^{\frac{E}{kT}} - 1} \mathrm{d}E \tag{2.22}$$

The rate of photon flux density emitting from the back surface is

$$R_{rad}^b = n_g^2 \overline{\epsilon_E^b} \int_{E_g}^{\infty} \frac{2\pi E^2}{h^3 c^2} \frac{1}{e^{\frac{E}{kT}} - 1} \mathrm{d}E \tag{2.23}$$

The unit of R_{rad}^f and R_{rad}^b are both #/s/cm^2.

The total photon-generation rate inside a solar cell with absorber thickness d in unit area is

$$R_{rad}^{total} = \mathrm{B}_0 n_i^2 d \tag{2.24}$$

where $\mathrm{B}_0 n_i^2$ is the radiative recombination per unit volume at equilibrium, and is related to the absorption coefficient α according to the van Roosbroeck-Shockley relation [8] in Eq. (2.25)

$$\mathrm{B}_0 n_i^2 = 4\pi \int_0^\infty \frac{2n_r^2 E^2}{h^3 c^2} \frac{\alpha}{e^{\frac{E}{kT}} - 1} \mathrm{d}E \tag{2.25}$$

The photon extraction (PE) factor from the front surface is:

$$\gamma_e^f = \frac{R_{rad}^f}{R_{rad}^{total}} = \frac{\overline{\epsilon_E^f} \int_{E_g}^\infty \frac{2\pi E^2}{h^3 c^2} \frac{1}{e^{\frac{E}{kT}} - 1} \mathrm{d}E}{d \frac{8\pi}{h^3 c^2} \int_0^\infty \frac{E^2 \alpha n_r^2}{e^{\frac{E}{kT}} - 1} \mathrm{d}E} = \frac{\overline{\epsilon_E^f} \int_{E_g}^\infty \frac{E^2}{e^{\frac{E}{kT}} - 1} \mathrm{d}E}{4\, d \int_0^\infty \frac{E^2 \alpha n_r^2}{e^{\frac{E}{kT}} - 1} \mathrm{d}E} \tag{2.26}$$

The PE factor from the back surface is:

$$\gamma_e^b = \frac{R_{rad}^b}{R_{rad}^{total}} = \frac{\overline{\epsilon_E^b} n_g^2 \int_{E_g}^\infty \frac{2\pi E^2}{h^3 c^2} \frac{1}{e^{\frac{E}{kT}} - 1} \mathrm{d}E}{d \frac{8\pi}{h^3 c^2} \int_0^\infty \frac{E^2 \alpha n_r^2}{e^{\frac{E}{kT}} - 1} \mathrm{d}E} = \frac{\overline{\epsilon_E^b} n_g^2 \int_{E_g}^\infty \frac{E^2}{e^{\frac{E}{kT}} - 1} \mathrm{d}E}{4\, d \int_0^\infty \frac{E^2 \alpha n_r^2}{e^{\frac{E}{kT}} - 1} \mathrm{d}E} \tag{2.27}$$

Neglecting the parasitic absorption in solar cell ($\gamma_l = 0$), the PR factor is

$$\gamma_r = 1 - \gamma_e^f - \gamma_e^b \tag{2.28}$$

The numerators of PE factors are bounded, but the denominators goes to infinity as the thickness increases, implying that PE factors approach to zero. Similarly, PR factor becomes unity as the thickness increases to infinity, and therefore B_{eff} will diminish to zero according to Eq. (2.21). Photon emission is proportional to the surface area, while photon generation is proportional to the volume of solar cell. As thickness of solar cell increases, photon generation will eventually significantly outweighs photon emission, making PR factor closes to unity.

2.4 Incorporation of Photon Recycling into the Drift-Diffusion Model

The detailed-balance model gives the maximum possible power conversion efficiency of a solar cell under ideal conditions. Numerical simulations based on solving the drift-diffusion equations can predict the performance of practical solar cells. The existence of the photon recycling (PR) effect is a hidden assumption in the detailed-balance model [6]. However, the drift-diffusion model does not consider it, and neither do most solar cell simulation software packages, including PC1D [9]. One method of incorporating PR effect into drift-diffusion model is to scale the radiative recombination coefficient B of the absorber layer material based on the sample geometry [10]. This method assumes that the quasi-Fermi level separation is constant throughout the absorber layer, which is a valid assumption for monocrystalline solar cells with a thickness close to, or shorter than, the diffusion length. In this section, the method of scaling B is applied to the simulation of CdTe/MgCdTe double-heterostructure solar cells. The detailed-balance model of a planar CdTe solar cell is developed. The cell structure is shown in Fig. 2-3. Reflectances of the front and back surfaces are referred to as R_f and R_b, respectively. The solar cell is either on a substrate or on a back-reflector. $R_b = 0$ in the case of absorbing substrate, and R_b can be close to unity if the back surface of the solar cell is coated with high quality metallic reflector.

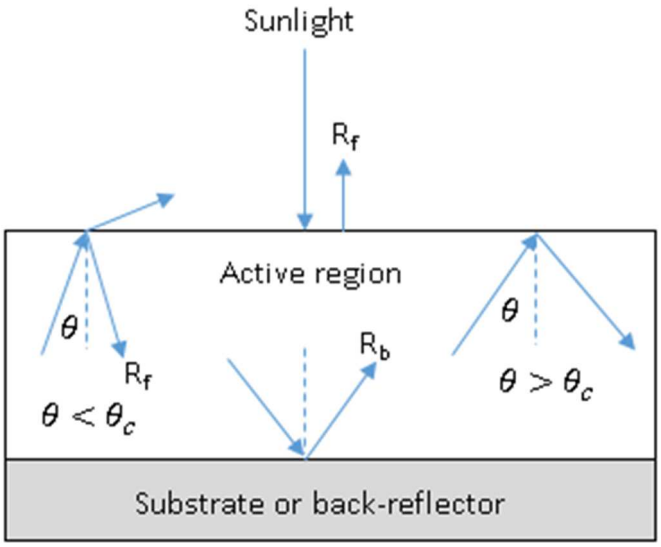

Fig. 2-3 Schematic Structure of a Planar Solar Cell, with Front and Back Surfaces Reflectances R_F and R_B.

Using ray-optics and taking into account of the incoherent multiple reflections between front and back surfaces, absorptance is:

$$\begin{aligned} A_E &= (1-R_f)\left[(1-e^{-\alpha d}) + e^{-\alpha d}R_b(1-e^{-\alpha d})\right. \\ &\quad \left. + e^{-2\alpha d}R_bR_f(1-e^{-\alpha d}) + \cdots\right] \\ &= (1-R_f)(1-e^{-\alpha d})(1+e^{-\alpha d}R_b)\frac{1}{1-R_bR_fe^{-2\alpha d}} \end{aligned} \tag{2.29}$$

The terms in the square bracket correspond to the absorption of the 1st, 2nd, 3rd,… light path in the solar cell.

Using Kirchhoff's law of thermal radiation or Eq. (2.5), the emittance of the front and back surfaces are:

$$\epsilon_E^f = n_r^2 \int_0^{\theta_c} \frac{(1-R_f)(1-e^{-\alpha d/\cos\theta})(1+e^{-\alpha d/\cos\theta}R_b)}{1-R_bR_fe^{-2\alpha d/\cos\theta}} 2\cos\theta\sin\theta\,\mathrm{d}\theta \quad (2.30)$$

and

$$\epsilon_E^b = \int_0^{\theta_c} \frac{(1-R_b)(1-e^{-\alpha d/\cos\theta})(1+e^{-\alpha d/\cos\theta}R_f)}{1-R_fR_be^{-2\alpha d/\cos\theta}} 2\cos\theta\sin\theta\,\mathrm{d}\theta + \int_{\theta_c}^{\frac{\pi}{2}} \frac{(1-R_b)(1-e^{-\alpha d/\cos\theta})(1+e^{-\alpha d/\cos\theta})}{1-R_be^{-2\alpha d/\cos\theta}} 2\cos\theta\sin\theta\,\mathrm{d}\theta \quad (2.31)$$

The derivation used the Helmholtz reciprocity principle, i.e. the absorbed light and the emitted light can be considered as the reversals of each other [4]. To simplify the analysis, R_f and R_b are assumed to be independent of photon energy, polarization, and angle.

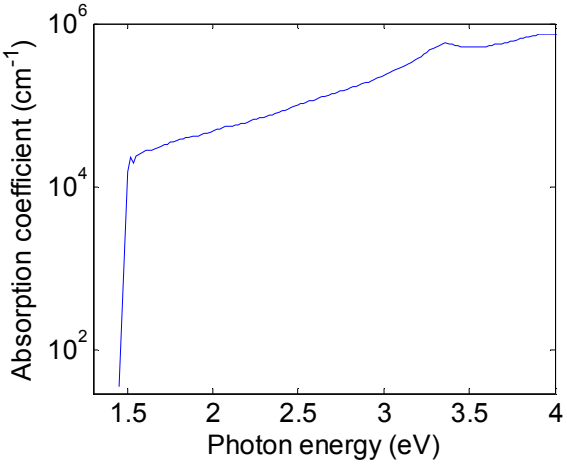

Fig. 2-4 Absorption Coefficient of Monocrystalline CdTe [11].

Plugging the absorption coefficient as shown in Fig. 2-4 into Eq. (2.29)-(2.31), and the parameters of d =1 μm, R_f = 2%, and R_b = 0, the absorptance and front and back

surface emittance of a CdTe solar cell are calculated and the results are shown in Fig. 2-5. The parameters are chosen as so to reflect the sample structure of the recently reported CdTe/MgCdTe DHs [12]. R_f is set to 2% because this value is readily achievable with state-of-the-art double layer anti-reflection coating (ARC) [13].

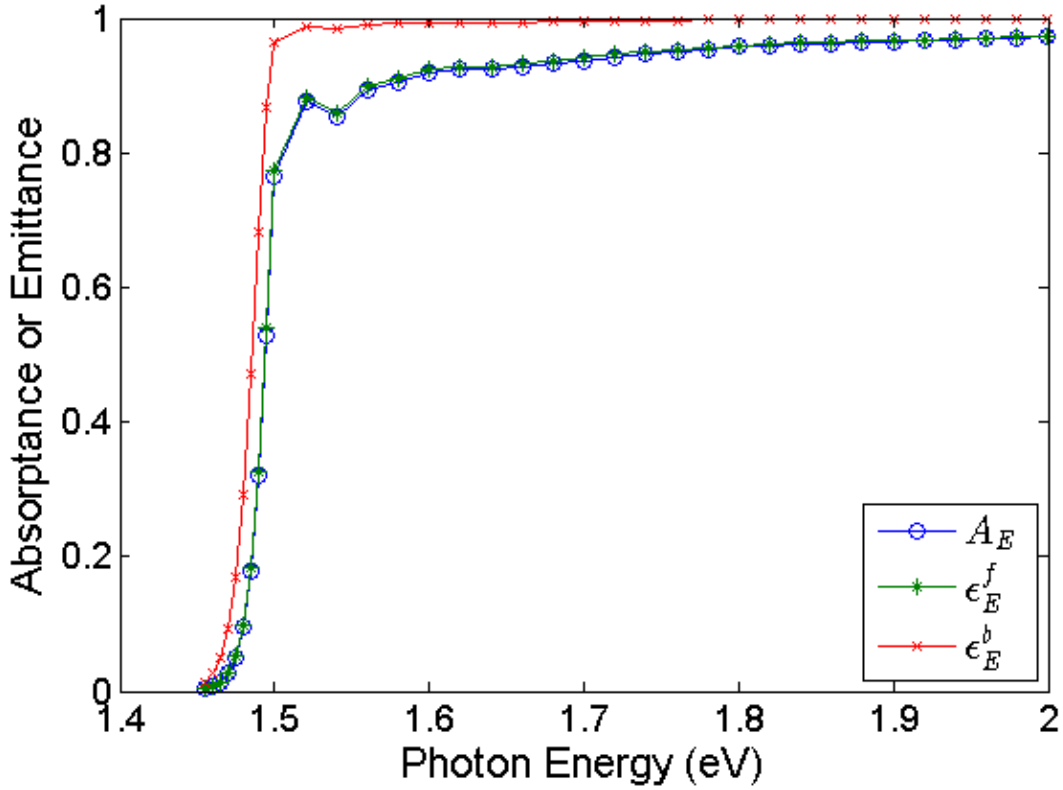

Fig. 2-5 Absorptance and Front and Back Surface Emittance of a CdTe Solar Cell, with Thickness of 1 μm, R_f = 2%, and R_b = 0.

The effective absorptance and effective emittances of front and back surfaces are calculated using Eq. (2.8), (2.17) and (2.18). The results are shown in Fig. 2-6. We can see that the effective absorptance increases with thickness and saturates around one, and the

effective emittances of both surface keep increasing as the thickness increases. Effective absorptance is larger than the effective emittance of front surface when the thickness is small (below 0.4 μm). The reason is that the effective absorptance characterizes the average absorptance on the solar spectrum; effective emittance characterizes the average emittance on the spontaneous emission spectrum. Spontaneous emission spectrum is around the bandgap energy where absorption coefficient is small; solar spectrum covers a large range above the bandgap where the absorption coefficient is large. Therefore, the effective absorptance is larger than the effective emittance of front surface. When the solar cell is thick (beyond 1 μm), the below bandgap emission takes over (the absorption coefficient of CdTe does not abruptly decreases to zero below the bandgap of 1.5 eV as seen from Fig. 2-4), making the emittances larger than one.

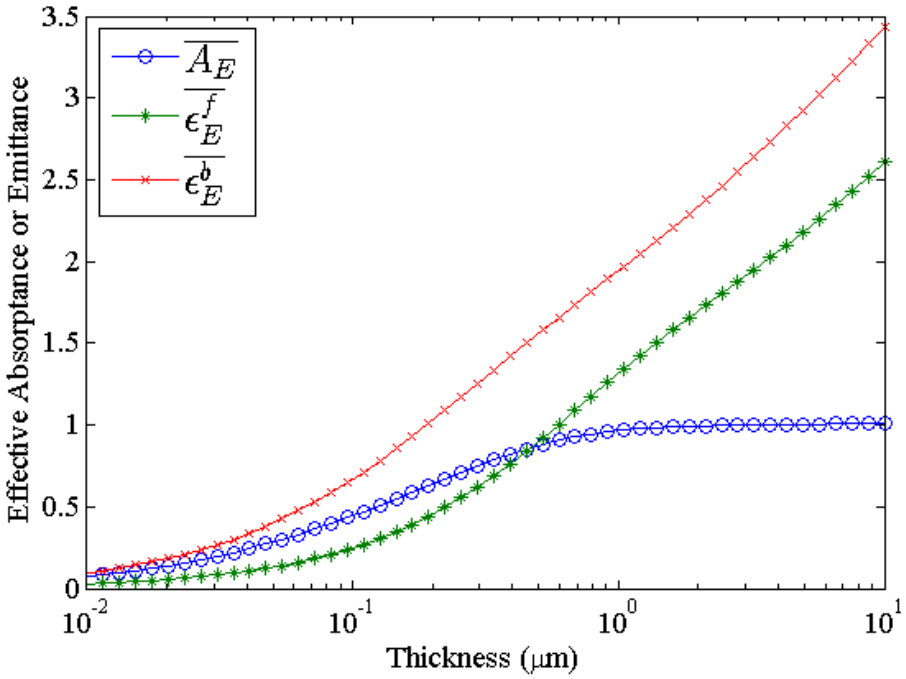

Fig. 2-6 Effective Absorptance and Effective Emittances of Front and Back Surfaces of CdTe Solar Cell as a Function of Thickness, with $R_f = 2\%$, and $R_b = 0$.

Using Eq. (2.26)-(2.35), PR and PE factors are calculated and shown in Fig. 2-7.

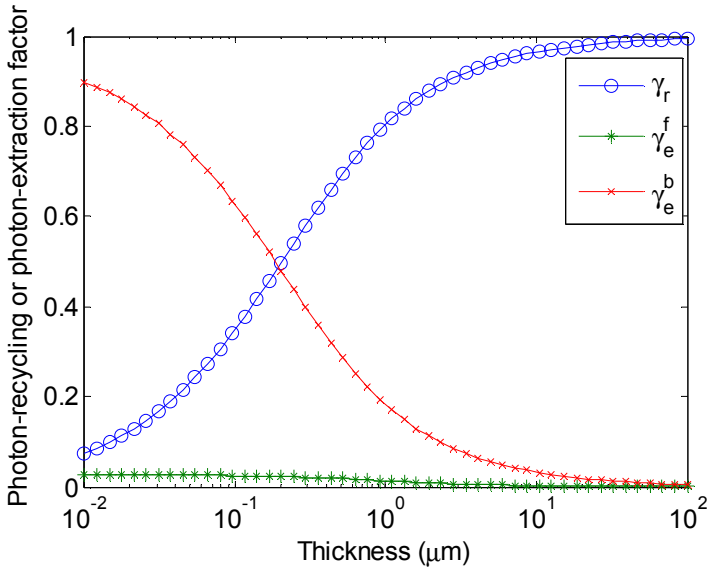

Fig. 2-7 PR Factor and PE Factors of Front and Back Surfaces as a Function of Thickness of CdTe Solar Cell, with R_f = 2%, and R_b = 0.

Numerical simulations using PC1D and the results of detailed-balance model are compared in Fig. 2-8. In the numerical simulation, carrier mobility is set to a very high value of 10^5 cm^2/(V·s), and non-absorbing passivation layers are used to make selective contacts to ensure that the carrier-collection efficiency is unity. Carrier lifetime is set to an extremely long value of 10^6 seconds to simulate the situation of zero non-radiative recombination. For the PC1D simulation with PR, the radiative recombination coefficient B of CdTe is set to B_{eff} using Eq. (2.21) and modified for each thickness; B is set to B_0 and left unchanged for the case of without PR. Results from the detail-balance model and the PC1D simulation are compared in Fig. 2-8. The three cases have the same J_{SC}, because the carrier-collection efficiencies are all unity. Detailed-balance model and the PC1D

simulation with PR have the same V_{oc} and efficiency, but the PC1D simulation results without PR deviate from the detailed-balance limit, implying that incorporating PR is necessary to simulate solar cell with efficiency approaching the detailed-balance limit. Without PR, PC1D simulations overestimate the radiative recombination in the solar cell, leading to lower V_{oc} and efficiencies than the detailed-balance limit.

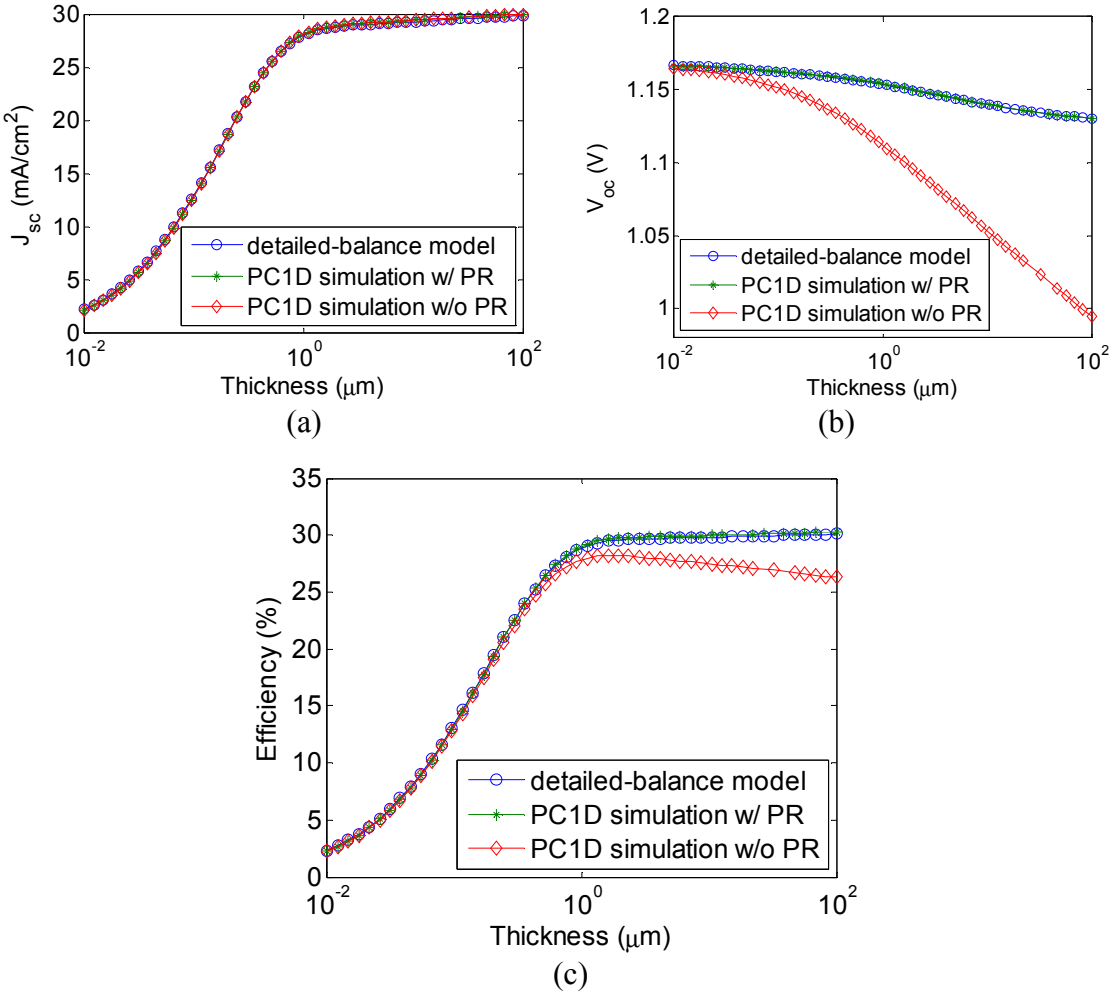

Fig. 2-8 Comparison of Detailed-Balance Limit and PC1D Simulation Results with and without Considering the Photon-Recycling (PR) Effect: (a)J_{SC}, (b)V_{OC}, and (c) Efficiency of CdTe Solar Cell vs. Absorber Thickness.

2.5 External Luminescence Quantum Efficiency

Efficient electron-to-photon conversion is a desirable material property for photovoltaic applications. The electron-to-photon conversion efficiency needs to be unity (purely radiative recombination) for solar cells to achieve the Shockley-Queisser limit [3]. A less-than-unity external luminescence quantum efficiency (η_{ext}) reduces the implied open-circuit voltage (iV_{oc}), or the quasi-fermi-level splitting in the absorber region, of solar cells, through the formula [13][14][15][16][17]:

$$V_{oc} = V_{db} + \frac{kT}{q}\ln(\eta_{ext}) \tag{2.32}$$

where V_{db} is the open-circuit voltage at the detailed-balance limit.

In fact, state-of-the-art solar cells are engineered to optimize light extraction to reach the highest possible efficiencies [16][17]. For example, by replacing the absorbing substrate with a reflective mirror, the η_{ext} of GaAs solar cell is improved from ~1% to over 20%, accompanied with a V_{oc} improvement of near 0.1 volt [13][16].

η_{ext} is the ratio of photons emitted out of the front surface to the electron and hole pairs radiative and non-radiative recombination at open-circuit, which is expressed as

$$\eta_{ext} = \frac{R_{rad}^{f}}{R_{rad}^{net} + R_{nr}} \tag{2.33}$$

where R_{rad}^{net} is the net radiative recombination taking into account the PR effect and is related to material's spontaneous emission rate R_{sp} as

$$R_{rad}^{net} = (1 - \gamma_r)R_{sp} \tag{2.34}$$

The spontaneous emission quantum efficiency η_{sp} is [7]:

$$\eta_{sp} = \frac{R_{sp}}{R_{sp} + R_{nr}} \tag{2.35}$$

where R_{nr} is the non-radiative recombination rate including the contributions from SRH, Auger, and surface recombination processes.

Rearranging the equations, the expression of the η_{ext} is obtained:

$$\eta_{ext} = \frac{\eta_{sp}\gamma_e^f}{1 - \eta_{sp}\gamma_r} \tag{2.36}$$

Define J_0^f as the radiative recombination current density emitting from the front surface at equilibrium:

$$J_0^f = q\overline{\epsilon_E^f}\int_{E_g}^{\infty} \frac{2\pi E^2}{h^3c^2}\frac{1}{e^{\frac{E}{kT}} - 1}\mathrm{d}E \tag{2.37}$$

J_0^f is related to the dark current density J_0 by

$$J_0^f = \eta_{ext}J_0 \tag{2.38}$$

Open circuit voltage is:

$$V_{oc} = \frac{kT}{q}\ln\left(\frac{J_{sc}}{J_0} + 1\right) \approx \frac{kT}{q}\ln\left(\frac{J_{sc}}{J_0}\right) = \frac{kT}{q}\ln\left(\frac{J_{sc}}{J_0^f}\right) + \frac{kT}{q}\ln(\eta_{ext}) \tag{2.39}$$

Denote $\frac{kT}{q}\ln\left(\frac{J_{sc}}{J_0^f}\right)$ by V_{db}, we arrive at the equation first proposed by R. T. Ross [14]:

$$V_{oc} = V_{db} + \frac{kT}{q}\ln(\eta_{ext}) \tag{2.40}$$

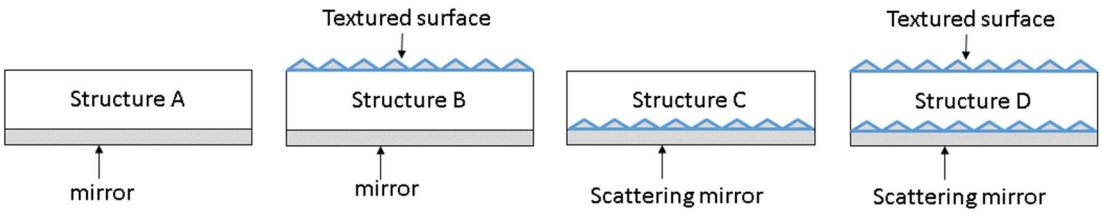

Fig. 2-9 Four Kinds of Solar Cell Structures.

Table 2-1 Summary of the Four Kinds of Solar Cell Structures.

Structures label		A	B	C	D
Front surface	Morphology	Smooth	Randomly textured	Smooth	Randomly textured
	Transmittance	1	1	1	1
	Transmittance distribution	Specular	Lambertian	Specular	Lambertian
Back surface	Morphology	Smooth	Smooth	Randomly textured	Randomly textured
	Reflectance	R_b	R_b	R_b	R_b
	Reflectance distribution	Specular	Specular	Lambertian	Lambertian

Consider four kinds of solar cell structures, as shown in Fig. 2-9. The properties of these structures are summarized in Table 2-1. All the cell structures have a mirror on the back surface with reflectance R_b. If $R_b = 0$, the solar cell is equivalent to having an absorbing substrate. On the other hand, the state-of-the-art thin-film solar cell has R_b close to unity. The back mirrors of A and B are smooth, providing specular reflection. The back mirrors of structure C and D are rough mirrors, scattering the reflected light to Lambertian distribution. Top surface of structure A and C are smooth, allowing normal incident light to go straight into the absorber. Top surface of structure B and D are textured, scattering incident light to Lambertian distribution. A perfect anti-reflection coating covers all the structures. Structure A represents the typical structure of thin-film GaAs solar cells [13]. Ultra-thin GaAs cell with textured back-reflector has structure C [18]. Structure B is a standard monocrystalline Si cell structure [19]. Structure D is a typical Silicon heterojunction cell structure [20].

Using ray-optics and taking into account of the incoherent multiple reflections between front and back surfaces, the surface absorptance and emittance of these structures are:

Structure A:

$$A_{E,A} = \left(1 - e^{-\alpha(E)d}\right)\left(1 + R_b e^{-\alpha(E)d}\right) \tag{2.41}$$

$$\epsilon_A^f = 1 - n_r^2 \int_0^{\theta_c} 2\sin\theta\cos\theta \left[(1 - R_b)e^{-\frac{\alpha(E)d}{\cos\theta}} + R_b e^{-\frac{2\alpha(E)d}{\cos\theta}}\right] \mathrm{d}\theta \tag{2.42}$$

$$\begin{aligned} \epsilon_A^b = &\int_0^{\theta_c} 2\sin\theta\cos\theta\,(1 - R_b)\left(1 - e^{-\frac{\alpha(E)d}{\cos\theta}}\right)\mathrm{d}\theta \\ &+ \int_{\theta_c}^{\frac{\pi}{2}} 2\sin\theta\cos\theta\,(1 - R_b)\frac{1 - e^{-\frac{2\alpha(E)d}{\cos\theta}}}{1 - R_b e^{-\frac{2\alpha(E)d}{\cos\theta}}}\mathrm{d}\theta \end{aligned} \tag{2.43}$$

Structure B:

$$A_{E,B} = \frac{x}{1 - y\left(1 - \frac{1}{n_r^2}\right)} \tag{2.44}$$

where

$$x = \int_0^{\frac{\pi}{2}} 2\sin\theta\cos\theta\left[1 - e^{-\frac{\alpha(E)d}{\cos\theta}}\right]\mathrm{d}\theta + \int_0^{\frac{\pi}{2}} 2\sin\theta\cos\theta\, e^{-\frac{\alpha(E)d}{\cos\theta}} R_b \left[1 - e^{-\frac{\alpha(E)d}{\cos\theta}}\right]\mathrm{d}\theta$$

and

$$y = \int_0^{\frac{\pi}{2}} 2\sin\theta\cos\theta\, R_b e^{-\frac{2\alpha(E)d}{\cos\theta}}\mathrm{d}\theta$$

$$\epsilon_{E,B}^f = A_{E,B} \tag{2.45}$$

$$\epsilon_{E,B}^b = (1 - R_b)\left[1 - t + t\left(1 - \frac{1}{n_r^2}\right)A_{E,B}\right] \tag{2.46}$$

where

$$t = \int_0^{\frac{\pi}{2}} 2\sin\theta\cos\theta\, e^{-\frac{\alpha(E)d}{\cos\theta}}\mathrm{d}\theta$$

Structure C:

$$A_{E,C} = 1 - e^{-\alpha(E)d} + e^{-\alpha(E)d}R_b x\frac{1}{1-R_b y} \tag{2.47}$$

$$\epsilon_{E,C}^{f} = n_r^2\int_0^{\theta_c} 2\sin\theta\cos\theta\left[1 - e^{-\frac{\alpha(E)d}{\cos\theta}} + e^{-\frac{\alpha(E)d}{\cos\theta}}R_b x\frac{1}{1-R_b y}\right]\mathrm{d}\theta \tag{2.48}$$

$$\epsilon_{E,C}^{b} = (1-R_b)x\frac{1}{1-R_b y} \tag{2.49}$$

where

$$\begin{aligned} x = &\int_0^{\theta_c} 2\sin\theta\cos\theta\left[1 - e^{-\frac{\alpha(E)d}{\cos\theta}}\right]\mathrm{d}\theta \\ &+ \int_{\theta_c}^{\frac{\pi}{2}} 2\sin\theta\cos\theta\left[1 - e^{-\frac{2\alpha(E)d}{\cos\theta}}\right]\mathrm{d}\theta \end{aligned} \tag{2.50}$$

and

$$y = \int_{\theta_c}^{\frac{\pi}{2}} 2\sin\theta\cos\theta\, e^{-\frac{2\alpha(E)d}{\cos\theta}}\mathrm{d}\theta \tag{2.51}$$

Structure D:

$$A_{E,D} = (1-x)(1+xR_b)\frac{1}{1 - x^2R_b\left(1 - \frac{1}{n_r^2}\right)} \tag{2.52}$$

$$\epsilon_{E,D}^{f} = A_{E,D} \tag{2.53}$$

$$\epsilon_{E,D}^{b} = (1-R_b)(1-x)\left[1 + x\left(1 - \frac{1}{n_r^2}\right)\right]\frac{1}{1 - x^2R_b\left(1 - \frac{1}{n_r^2}\right)} \tag{2.54}$$

where

$$x = \int_0^{\frac{\pi}{2}} 2 \sin\theta \cos\theta e^{-\frac{\alpha(E)d}{\cos\theta}} \, d\theta \tag{2.55}$$

Consider GaAs solar cells in the four structures. The thicknesses required to obtain an absorptance of 99% as a function of reflectance of the back-reflector are shown in Fig. 2-10. The thickness indicates the performance of light trapping of the four structures. With great light trapping, the required thickness is reduced. The thicknesses decrease monotonically with mirror reflectance. Performance of structure B and D are almost identical and are both better than A and C. When the reflectance is small, structure A and C have similar performance. The performance of C catches up with B and D when the reflectance is close to unity.

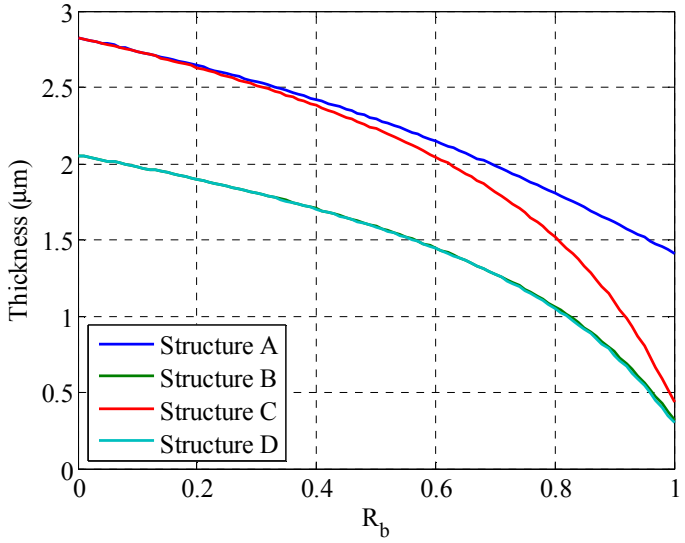

Fig. 2-10 Thickness Required to Obtain 99% Effective Absorptance.

Due to the one-to-one relationship between V_{oc} and η_{ext} in Eq. (2.40), the bigger the η_{ext}, the higher the V_{oc}. Since all the four structures have 99% absorptance, J_{sc} are the

same. The IV curves have the same functional relationship, i.e. the bigger the η_{ext}, the higher the power conversion efficiency of the solar cell. η_{ext} as a function of spontaneous emission quantum efficiency η_{sp} is shown in Fig. 2-11. When η_{sp} is small, the asymptotic expression of η_{ext} is $\eta_{ext} = \gamma_e \eta_{sp}$ according to Eq. (2.36), which explains the linear behavior of the curves when η_{sp} is small. As η_{sp} increases and approaches unity, PR effect comes into play, and reduces the denominator in Eq. (2.36), and causes the upward bending of η_{ext} on the right as shown in Fig. 2-11 (a) and (b). When η_{sp} is the same, i.e. the same material quality, structure B and D have similar η_{ext}, and both of which outperform C, and then A. Therefore, η_{ext} correlates well with performance of light-trapping (see Fig. 2-10), as a results of the reciprocity of light absorption and emissions. Comparing Fig. 2-11 (a) and (b), solar cells with a perfect back-reflector outperform the cells with a poor back-reflector.

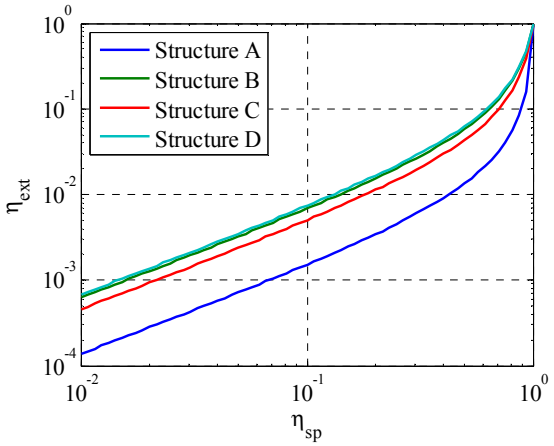

(a) $R_b = 1$

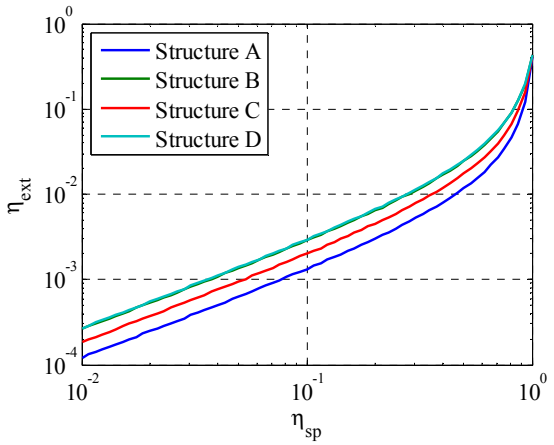

(b) $R_b = 0.9$

Fig. 2-11 External Luminescence Quantum Efficiency (η_{ext}) as a Function of Spontaneous Emission Quantum Efficiency when (a) $R_b = 1$ and (b) $R_b = 0.9$.

η_{ext} as a function of R_b is shown in Fig. 2-12. The solid and dashed lines show the results when η_{sp}= 0.9 and η_{sp}= 0.99, respectively. As expected, η_{ext} increases with η_{sp}. There is an upward bending of the η_{ext} as R_b approaches unity, indicating the importance of a good back-reflector.

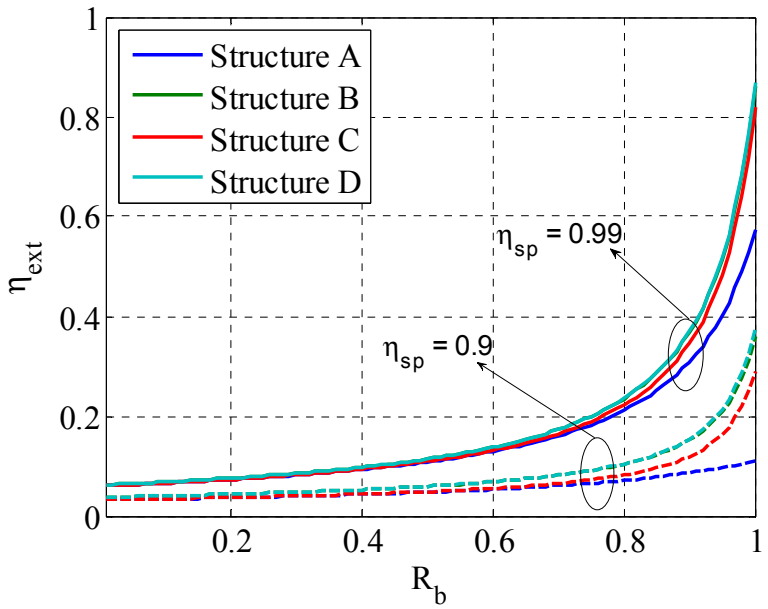

Fig. 2-12 External Luminescence Quantum Efficiency (η_{ext}) as a Function of Reflectance.

2.6 Summary of Chapter

This chapter summarized the detailed-balance model of solar cells with finite thickness. PC1D simulation including photon recycling (PR) by adjusting the radiative recombination coefficient B was carried out. The validity of the method is verified by comparing the detailed-balance limit and the drift-diffusion model with no non-radiative recombination. PC1D simulation including PR effect yields the same results as the detailed-balance limit. The PC1D simulation without PR effect gives incorrect results. It is therefore important to include PR when simulating solar cell approaching the radiative limit. The External Luminescence Quantum Efficiency (η_{ext}) has been introduced. The η_{ext} of GaAs solar cells with various structures have been calculated and compared.

CHAPTER 3

THE INFLUENCE OF BELOW-BANDGAP ABSORPTION ON SOLAR CELL EFFICIENCY

3.1 Introduction

The Shockley-Queisser (S-Q) model [3] assumes that the absorptance spectrum of a solar cell is a Heaviside step-function centered at the bandgap energy, i.e. zero below and unity above the bandgap. The absorptance of a practical solar cell is always non-zero below the absorber bandgap. Assuming the sun as a diluted 6000 K black-body radiation source, the optimum bandgap, and the S-Q limit of a single-junction solar cell are calculated as 1.3 eV and 31%, respectively. However, in reality, solar cell absorbers possess below-bandgap absorption. For example, the Urbach tail of bulk semiconductors makes the absorptance an exponential decay function below the bandgap. This chapter studies the impact of the below-bandgap absorption on the performance of solar cells.

The exponential decay of the absorption coefficient below the bandgap, known as the Urbach tail [21], has been widely observed in alkali halides, II-VI, III-VI, and group IV semiconductors, organics, and amorphous materials [22][23][24][25]. The origin of this phenomenon is mainly attributed to phonon assisted excitation [23][25], or ionizing electric fields caused by phonons, impurities, and composition fluctuations in alloys [22]. The absorption coefficient in the Urbach tail as a function of the photon energy E is expressed as [26]:

$$\alpha(E) = \alpha_g \exp\left(\frac{E - E_g}{E_u}\right) \tag{3.1}$$

where E_g is the bandgap energy, α_g is the absorption coefficient at E_g, and E_u is the Urbach tail width, which characterizes the slope of the exponential decay.

On the one hand, the Urbach tail enhances the total absorption and thus increases the short-circuit current density. On the other hand, it reduces the open-circuit voltage due to a smaller effective bandgap. It is thus important to include the Urbach tail in the modeling to draw accurate predictions of solar cell performance.

Because of the existence of the Urbach tail, for a practical solar cell device, the absorptance spectrum is a continuous function rather than a step-function as the S-Q model assumes. This chapter attempts to answer the following questions: what is the maximum efficiency of a solar cell when the Urbach tail is present? Is it possible that this maximum efficiency exceeds that of a solar cell without the Urbach tail, or even the S-Q limit achieved at the optimum bandgap? What is the optimum absorptance spectrum to achieve the maximum efficiency of a single-junction solar cell?

3.2 Detailed-Balance Efficiency Limit of Solar Cells with Urbach Tails

Consider a planar solar cell with an ideal reflector on the back surface. The sunlight is normally incident on the front surface. Radiative recombination is assumed to be the only recombination mechanism in the solar cell. Based on the formulism given in reference, various parameters and device performance can be calculated or derived as follows.

The short-circuit current density J_{sc} for a solar cell is determined by the number of absorbed photons:

$$J_{sc} = q\int_0^{\infty} A(E)\Phi_{sun}(E)\,\mathrm{d}E \tag{3.2}$$

where E is the photon energy; $A(E)$ is the spectral absorptance of the solar cell, defined as the percentage of light absorbed as a function of photon energy E; $\phi_{sun}(E)$ is the photon flux density of solar radiation, which is approximated as a diluted 6000 K black-body radiation with a dilution factor of:

$$f_{\omega} = \left(\frac{D}{2L}\right)^2 \tag{3.3}$$

where $D = 1.392 \times 10^6$ km is the diameter of the sun, and $L = 1.496 \times 10^8$ km is the distance from the sun to the earth.

The radiative recombination current density is related to the forward-bias voltage V through:

$$J_{Rad}(V) = J_0\left[\exp\left(\frac{qV}{kT_C}\right) - 1\right] \tag{3.4}$$

where J_0 is the dark current density determined by the thermal radiation at equilibrium, and is expressed as:

$$J_0 = q\int_0^{\infty} \epsilon(E)\Phi_{bb}(T_c, E)\mathrm{d}E \tag{3.5}$$

where T_c is the temperature of the solar cell, usually assumed to be 300 K, unless stated otherwise; $\epsilon(E)$ is the emittance of the solar cell, which is the ratio of emitted photon flux density to that of a black-body. $\Phi_{bb}(T_c, E)$ is the photon flux density of a black-body (# of photons per unit area, per unit energy interval, per time).

$$\Phi_{bb}(T_c, E) = \frac{2\pi E^2}{h^3 c^2} \frac{1}{e^{\frac{E}{kT_c}} - 1} \tag{3.6}$$

According to Kirchhoff's law of thermal radiation at equilibrium, the emittance equals absorptance at any photon energy, or

$$A(E) = \epsilon(E) \tag{3.7}$$

The output current and power densities of a solar cell in the detailed-balance model are:

$$J(V) = J_{sc} - J_{Rad}(V) \tag{3.8}$$

$$P(V) = JV = (J_{sc} - J_{Rad}(V))V \tag{3.9}$$

The absorptance spectra for solar cells made of common PV materials and with typical thicknesses, calculated using published absorption coefficients [26][27][28][29], are shown in Fig. 3-1. All of the cells are assumed to have perfect anti-reflection coatings and ideal back-reflectors, and therefore the absorptance is calculated as:

$$A(E) = 1 - \exp[-2\alpha(E)d] \tag{3.10}$$

where *d* is the absorber thickness.

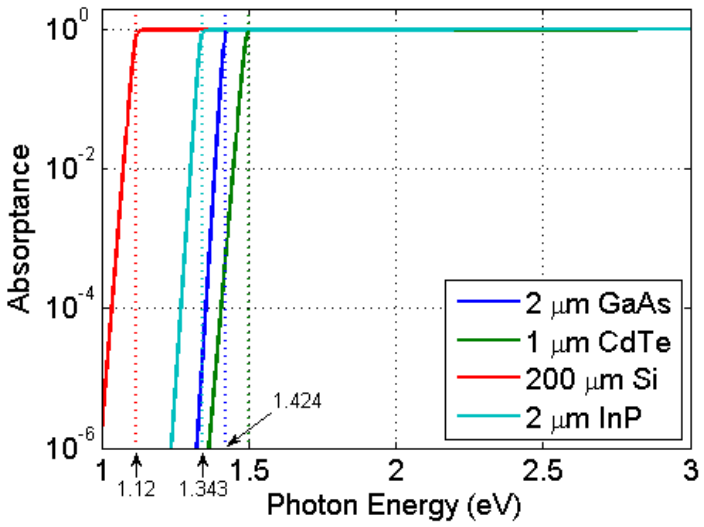

Fig. 3-1 Absorptance Spectra of 2 μm Thick GaAs, 1 μm Thick CdTe, 200 μm Thick Silicon, and 2 μm Thick InP Solar Cells.

According to Fig. 3-1, the absorptance is almost unity above the bandgap, and decreases exponentially below it. The decay factor is equal to the Urbach tail width E_u of the material. Therefore, we consider a simplified absorptance spectrum, as shown below, for the rest of this paper.

$$A(E) = \begin{cases} 1 & E \geq E_g \\ \exp\left(\dfrac{E - E_g}{E_u}\right) & E < E_g \end{cases} \tag{3.11}$$

Plugging the absorptance spectrum $A(E)$ into the expressions of J_{sc} and J_0, the I-V curve of the solar cell under the detailed-balance limit can be calculated. The J_{sc}, J_0, open-circuit voltage V_{oc}, and the cell efficiency versus the decay factor E_u for solar cells with bandgaps of 1.1 eV, 1.3 eV, and 1.9 eV are shown in Fig. 3-2. As shown in Fig. 3-2 (a), J_{sc} increases linearly with E_u, because the absorption tail reduces the effective bandgap

to $E_g - E_u$ [4]. However, J_0 increases exponentially with E_u as shown in Fig. 3-2 (b). When E_u is smaller than the room temperature thermal energy kT_c, J_0 is increased by a factor of $e^{\frac{E_u}{kT_c}}$ [4]. J_0 is the integral of emittance times the room-temperature black-body radiation. Below the bandgap, emittance decreases exponentially at a rate of E_u, while black-body radiation increases exponentially at a rate of kT_c. When E_u is larger than kT_c, the product of the two exponential terms does not converge to zero, which explains the faster increase of J_0 beyond kT_c. V_{oc} versus E_u is shown in Fig. 3-2 (c), where V_{oc} decreases monotonically with E_u. The impact of E_u on the cell efficiency is shown in Fig. 3-2 (d), which reveals the following:

1. The solar cell efficiency decreases monotonically with E_u for the cells with bandgaps lower than 1.3 eV.
2. The efficiency increases slightly as E_u increases at first and then decreases for the cells with a bandgap larger than 1.3 eV.
3. With a very large E_u, solar cells with a wider bandgap may have a slightly higher efficiency than that of the same cells without Urbach tail states.

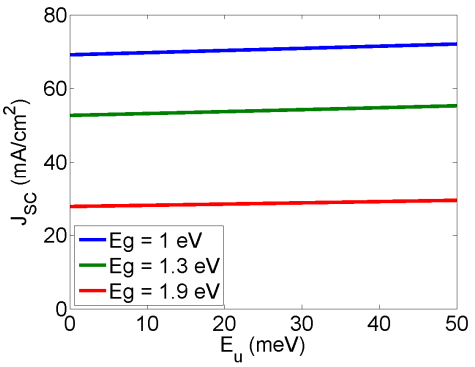

(a)

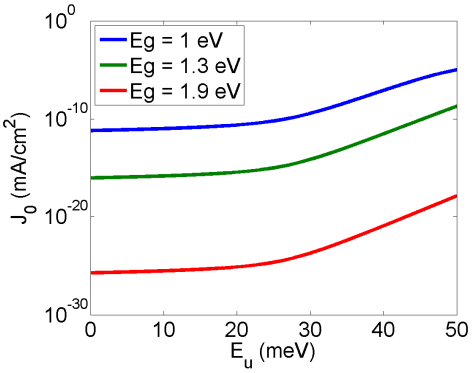

(b)

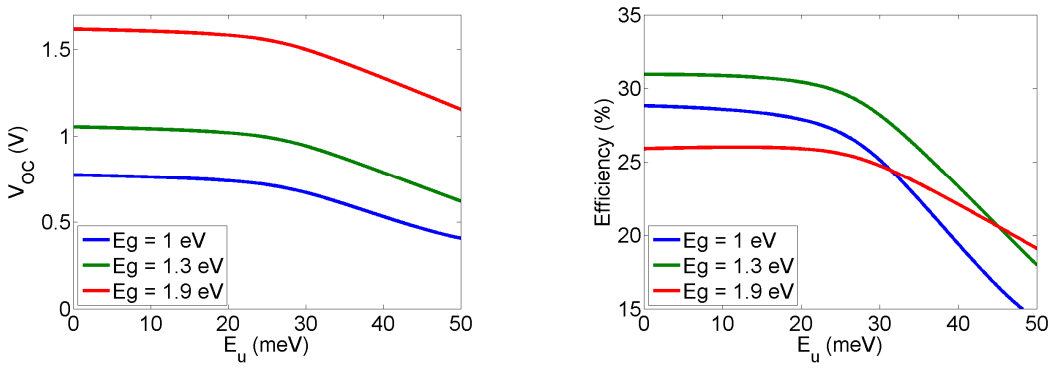

(c) (d)

Fig. 3-2 J_{sc} (a), J_0 (b), V_{oc} (c), and Efficiency (d) as Functions of E_u for Solar Cells with Different Bandgaps Under the Diluted 6000 K Black-Body Radiation and a Cell Temperature of 300 K.

The optimum E_u, and the maximum efficiency improvement compared to $E_u = 0$ (step-function absorptance spectra) as functions of the bandgap are shown in Fig. 3-3. When the bandgap is less than 1.3 eV, i.e. the optimum bandgap of the S-Q model, the optimum E_u is zero, meaning that any Urbach tail would decrease the efficiency. The optimum E_u becomes non-zero and increases with bandgap when the bandgap is larger than 1.3 eV. The calculations show that the maximum enhancement of the efficiency is only 0.17%, which is achieved by a solar cell with E_g=2.57 eV and E_u=17.4 meV. However, the cell efficiency is only 16.2%, much smaller than the S-Q limit. Although the efficiency can be enhanced due to the Urbach tail for solar cells with bandgaps greater than 1.3 eV, the enhanced efficiency is always smaller than the S-Q limit.

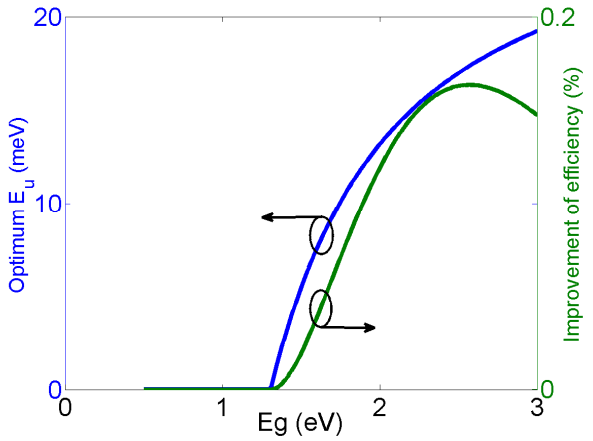

Fig. 3-3 Optimum Absorption-Tail Width E_u and the Corresponding Maximum Improvement of Efficiency as Functions of Bandgap.

3.3 The Optimum Absorptance Spectrum

Can the efficiency of the solar cell with an Urbach tail, or any other absorptance spectral features, beat the S-Q limit? This section answers this question by finding out the optimum absorptance spectrum of solar cells that gives the maximum efficiency.

The output power of the solar cell is:

$$P(V) = V\left(\int_0^\infty qA(E)\Phi_{sun}(E)\mathrm{d}E - J_0\left[\exp\left(\frac{qV}{kT_C}\right) - 1\right]\right) \tag{3.12}$$

Since $\epsilon(E)$ equals absorptance $A(E)$ under equilibrium according to the Kirchhoff's law of thermal radiation, and thus the expression of the dark current density J_0 is:

$$J_0 = q\int_0^\infty A(E)\Phi_{bb}(T_c, E)\mathrm{d}E \tag{3.13}$$

Also, $\exp\left(\frac{qV}{kT_c}\right) \gg 1$ since the operating voltage V of a solar cell is usually much larger than the thermal voltage $\frac{kT_c}{q}$. The expression of the output power is:

$$P(V) = qV \int_0^{\infty} A(E) \left[\Phi_{sun}(E) - \exp\left(\frac{qV}{kT_c}\right) \Phi_{bb}(T_c, E)\right] \mathrm{d}E \tag{3.14}$$

The highest output power under certain operating voltage V is obtained when the integral is maximized. In the integral, $\Phi_{sun}(E)$ is the photon flux density of solar radiation, and $\exp\left(\frac{qV}{kT_c}\right) \Phi_{bb}(T_c, E)$ is the photon flux density of black-body radiation at cell temperature T_c under operating voltage V, both of which are plotted in Fig. 3-4.

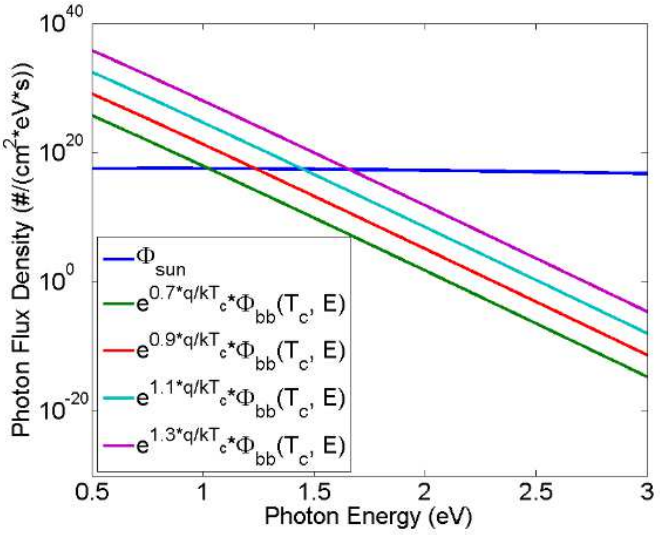

Fig. 3-4 Comparison between Photon Flux Densities of Solar Radiation and Radiative Recombination Losses under Different Voltages.

For a cell working at a fixed voltage V, on the one hand if:

$$\Phi_{sun}(E) - \exp\left(\frac{qV}{kT_c}\right)\Phi_{bb}(T_c, E) > 0 \tag{3.15}$$

increasing $A(E)$ will boost the output power.

On the other hand, if:

$$\Phi_{sun}(E) - \exp\left(\frac{qV}{kT_c}\right)\Phi_{bb}(T_c, E) < 0 \tag{3.16}$$

reducing $A(E)$ will improve the output power.

Since the range of values of the absorptance $A(E)$ is [0, 1], the maximum power is obtained when:

$$A(E) = \begin{cases} 1, & if\ \Phi_{sun}(E) - \exp\left(\frac{qV}{kT_c}\right)\Phi_{bb}(T_c, E) \geq 0 \\ 0, & if\ \Phi_{sun}(E) - \exp\left(\frac{qV}{kT_c}\right)\Phi_{bb}(T_c, E) < 0 \end{cases} \tag{3.17}$$

According to Fig. 3-4, $\exp\left(\frac{qV}{kT_c}\right)\Phi_{bb}(T_c, E)$ is larger than $\Phi_{sun}(E)$ at lower photon energies, and smaller than $\Phi_{sun}(E)$ at higher photon energies. The curves $\Phi_{sun}(E)$ and $\exp\left(\frac{qV}{kT_c}\right)\Phi_{bb}(T_c, E)$ intersect at energy E_1, which is the solution to the following equation:

$$\Phi_{sun}(E_1) - \exp\left(\frac{qV}{kT_c}\right)\Phi_{bb}(T_c, E_1) = 0 \tag{3.18}$$

Then the optimum absorptance spectrum is a step-function:

$$A(E) = \begin{cases} 1, & if\ E \geq E_1 \\ 0, & if\ E < E_1 \end{cases} \tag{3.19}$$

Therefore, at any operating voltage V, the maximum output power is achieved if the absorptance spectrum is a step-function, and the "cutoff" photon energy E_1 is the

solution to (2.5). Also, it is well-known that, according to the S-Q model [3], the S-Q limit is the maximum efficiency of a single-junction solar cell assuming a step-function absorptance spectrum. However, the model does not predict efficiency limit when the absorptance is not a step function. Hence, in light of the discussion given above, we can conclude that the S-Q limit is the maximum efficiency limit for single-junction solar cells with any kinds of absorptance spectra. In another word, the efficiency of a solar cell with below-bandgap absorption, regardless of the absorptance spectral feature, cannot beat the S-Q limit.

3.4 Summary of Chapter

The impact of the below-bandgap absorption on the solar cell performance has been studied. The Urbach tail has been found to slightly increase the short-circuit current density and significantly magnify the dark current density. If the bandgap is smaller than the optimum value given by the Shockley-Queisser (S-Q) model, the presence of the Urbach tail has a negative impact on the efficiency. The Urbach tail can increase the efficiency only when the bandgap is larger than the optimum value of 1.3 eV. However, the efficiency improvement is insignificant, with a maximum increase of 0.17%. It is found that the efficiency increases as the absorptance spectrum approaches a step-function. In fact, regardless of the shape of the below-bandgap absorptance spectrum, the maximum efficiency is always lower than the S-Q limit, which is achieved by a step-function absorptance spectrum with the optimum bandgap. It has been proved that any deviations

from the optimum step-function absorptance spectrum will result in a lower efficiency than the S-Q limit.

CHAPTER 4

RADIATIVE RECOMBINATION DOMINATED N-TYPE CdTe/MgCdTe DOUBLE-HETEROSTRUCTURES

4.1 Introduction

This chapter reviews the technologies of thin-film CdTe solar cells. A major challenge for CdTe thin-film cell is the problem of low V_{oc}, due to the short carrier lifetime and low p-type doping in the polycrystalline CdTe absorber. It is non-radiative recombination that dominates the recombination processes in the poly-CdTe absorbers.

The MBE optoelectronics group at Arizona State University has significantly improved the material quality and carrier lifetime in monocrystalline CdTe/MgCdTe double-heterostructures (DHs). CdTe can be easily doped n-type using Indium-doping. The photoluminescence quantum efficiency (PLQE) measurement is conducted to quantify the ratio of radiative recombination to total recombination events. A maximum external luminescence quantum efficiency (η_{ext}) of 3.1% under one-sun condition is observed from a 1-μm-thick CdTe/MgCdTe DH sample with the optimum doping level. Such a high efficiency gives an implied open-circuit voltage (V_{oc}), or quasi-Fermi-level splitting, of 1.13V.

4.2 Review of Thin-Film CdTe Solar Cell Technologies

Thin-film solar cells are fabricated by depositing photovoltaic (PV) thin-films on low-cost substrates such as glass, metal, or plastic. The total thickness of the thin-films is no more than a few microns, compared to silicon wafers that are up to hundreds of microns

thick. Some commercialized thin-film solar cell technologies include CdTe, copper indium gallium selenide (CIGS), or amorphous thin-film silicon (a-Si).

Backed by the company, First Solar, several gigawatts (GW) of polycrystalline CdTe-based thin-film solar cell modules are manufactured each year. The success of the thin-film CdTe technology is reliant on the superb optical properties of CdTe for the photovoltaic (PV) application:

(1) Near optimum bandgap of about 1.5 eV (monocrystalline CdTe has a bandgap of 1.5 eV while p-type CdTe films has a bandgap of 1.45 eV due to defect absorptions [30]).
(2) High absorption coefficient of over 15000 cm^{-1} at the band edge [11].

The detailed-balance limiting efficiency is 32.1% under AM1.5G conditions assuming the cell has an ideal back-reflector [3]. As shown in Fig. 4-1 and Table 4-1, CdTe has a similar limiting efficiency compared to Silicon and GaAs. A unique feature of CdTe is that the absorption coefficient at the bandgap energy is much higher than that of Silicon and GaAs. This property is key to thin-film PV applications. In fact, a 1-μm-thick CdTe absorber is able to absorb 98% of the above-bandgap-photons.

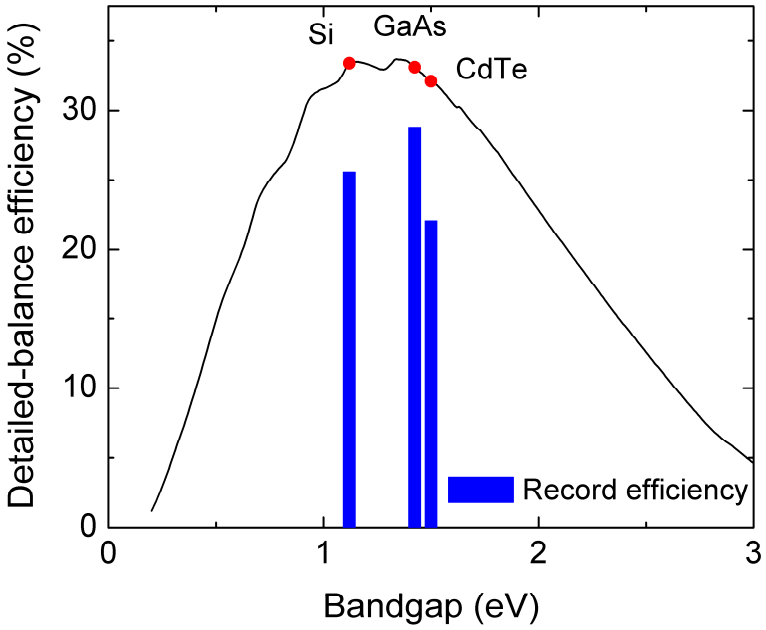

Fig. 4-1 Detailed-Balance Efficiency as a Function of Bandgap under the AM1.5G Spectrum. The Record Efficiencies of Si, GaAs, and CdTe Cells are Compared.

Table 4-1 Material Properties of Some Common Photovoltaic Materials

PV material	**Eg (eV)**	**Detailed-balance efficiency**	**Record cell efficiency**	**Absorption coefficient at Eg, α (cm^{-1})**	**Absorption depth, 1/α (μm)**
Si	1.12	33.4%	25.6%	4.0	2500
GaAs	1.424	33.1%	28.8%	8280	1.21
CdTe	1.5	32.1%	22.1%	15200	0.658

The evolution of the record thin-film CdTe cell efficiency is shown in Fig. 4-2. From the figure, we can see three leaps in the record efficiencies.

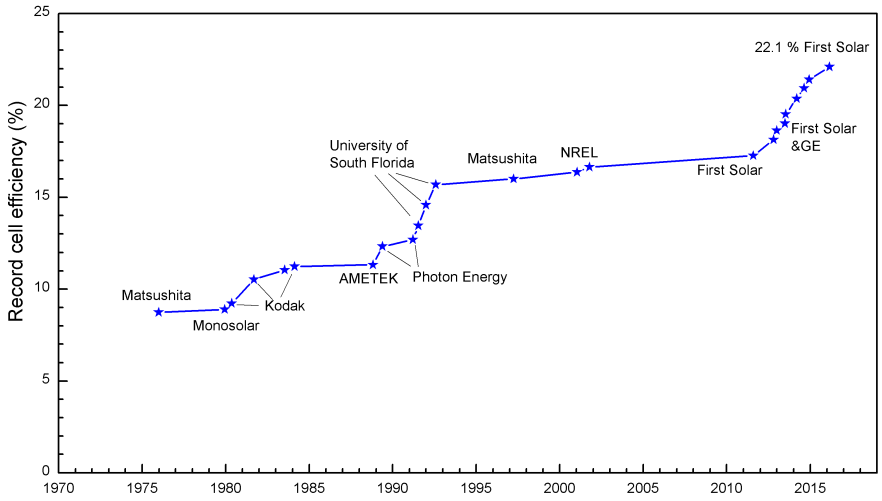

Fig. 4-2 Record Thin-Film CdTe Solar Cell Efficiencies.

The first leap happened in the early 1980s when Kodak pushed the cell efficiencies over 10%. Polycrystalline thin-film CdS/CdTe solar cells were deposited on glass by the close space sublimation (CSS) method and the oxygen treatment was discovered to enhance the performance [31]. In CSS chamber, the CdTe source and the substrate, having the same size, are brought into close proximity. During the deposition, the CdTe source is heated to a higher temperature than the substrate so that the CdTe material diffuses from the source to the substrate [32].

The second breakthrough occurred in the early 1990s. University of South Florida pushed the thin-film CdS/CdTe cell efficiency to 15.8% [33]. The cell structure is shown in Fig. 4-3, CdS film was prepared by chemical bath deposition and the CdTe film was deposited by CSS. After the thin-film depositions, $CdCl_2$ [34] and heat treatments [30] were used to improve the cell performance.

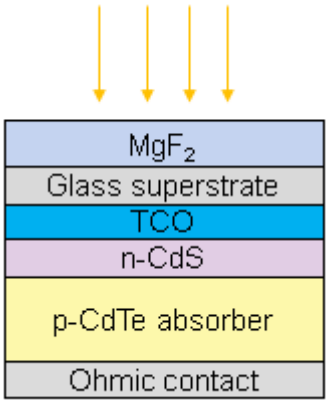

Fig. 4-3 Layer Structure of Thin-Film CdS/CdTe Solar Cells [33].

Around the year 2000, researchers from NREL (National Renewable Energy Laboratory) incorporated a high resistance transparent (HRT) layer between the transparent conducting oxide (TCO) layer and the CdS layer, as shown in Fig. 4-4, improving the performance and reproducibility of CdTe solar cells [35]. In the study, the TCO and HRT materials are Cadmium Stannate (Zn_2SnO_4, or CTO), and Zinc Stannate (Zn_2SnO_4, or ZTO), respectively.

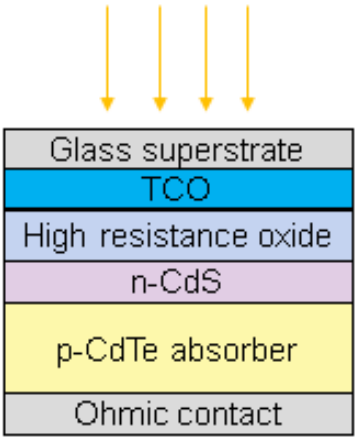

Fig. 4-4 CdTe Solar Cell Structure with a High Resistance Layer [32].

The third major breakthrough was made possible by First Solar and GE (General Electric) in the recent years, pushing the record cell efficiency to 22.1% by February 2016 [36]. The detailed cell structure is not known to the public. The use of a copper-doped p-type Zinc Telluride (ZnTe) back-contact layer may be responsible for the rapid improvement of efficiencies [37][38]. The resulting structure is a lightly doped p-CdTe absorber sandwiched between heavily doped n-type CdS and p-type ZnTe, which act as the electron- and hole-contact layers, respectively.

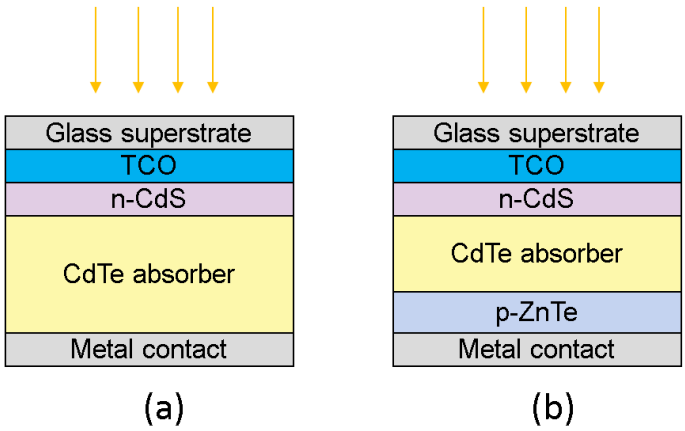

Fig. 4-5 Comparison of the Standard Device (a) and the ZnTe-Based Device (b) from First Solar [37].

In summary, the last twenty years have seen significant improvement of CdTe cell efficiencies. Table 4-2 summarizes the I-V parameters of the record-efficiency CdTe solar cells. The J_{sc} improved from 25.1 mA/cm^2 to 30.25 mA/cm^2, a 20.5% relative increase. The fill-factor (FF) improved from 74.5% to 80%, a 7.4% relative increase. The V_{oc} improved from 843 mV to 875.9 mV, only a 3.9% relative increase. Note that the maximum

J_{sc} of polycrystalline CdTe (all the photons above the bandgap of 1.45 eV, ignoring below-bandgap absorptions) is 30.84 mA/cm^2. The record-efficient cell collects 98% of the maximum J_{sc}. The FF of 79.4% is also a decent value. The highest V_{oc} of 875.9 mV is 574 mV below the CdTe bandgap of 1.45 eV, and 304 mV below the detailed-balance limit of 1.18 V. The low V_{oc} is attributed to the large non-radiative recombination inside of, and at the boundary of the polycrystalline CdTe absorbers, where the carrier lifetime is only tens of nanoseconds [39].

Table 4-2 Record-Efficient CdTe Cell I-V Parameters [39].

Year	Team	Efficiency (%)	V_{oc} (mV)	J_{sc} (mA/cm^2)	FF (%)
1993	USF	15.8	843	25.1	74.5
1997	Matsushita	16	840	26.1	73.1
2001	NREL	16.4	848	25.9	74.5
2001	NREL	16.7	845	26.1	75.5
2011	FSLR	17.3	845	27	75.8
2012	GE	18.3	857	27	79
2013	FSLR	18.7	852	28.6	76.7
2013	FSLR	19	872	28	78
2013	GE	19.6	857.3	28.59	80
2014	FSLR	21	875.9	30.25	79.4

Research on monocrystalline CdTe solar cells has been conducted to study the material properties of CdTe, and to close the gap between the best research cell and the detailed-balance limit. J. M. Burst, et al. [40] deposited n-type CdS window layer on p-type CdTe wafers to make monocrystalline CdS/CdTe solar cells, achieving V_{oc} over 1 V.

The high voltage is attributed to improved material quality and increased p-type doping level in CdTe. The maximum efficiency of monocrystalline CdTe solar cell is 15.2%, which is still lower than the polycrystalline thin-film cells.

4.3 High Quality CdTe/MgCdTe DHs Grown on InSb Substrates

In 1993, A. Waag et al. [41] first reported the epitaxial growth of Magnesium Telluride (MgTe) and the ternary alloy $Mg_xCd_{1-x}Te$ on CdTe substrate. The lattice constant of MgTe is 6.435 ± 0.002 Å, only 0.7% smaller than that of CdTe. The CdTe/$Mg_xCd_{1-x}Te$ quantum wells (QWs) were then grown [42]. The band alignment between CdTe and $Mg_xCd_{1-x}Te$ is type-I with a valence band-offset of 30 %. In 1981, R. F. C. Farrow et al. reported the MBE (Molecular Beam Epitaxy) growth of CdTe epilayers on InSb (001) substrates [43]. The lattice-mismatch between CdTe and InSb is only 0.025%. As a comparison, the lattice-mismatch between the widely-used GaAs/AlAs heterostructure is 0.1%.

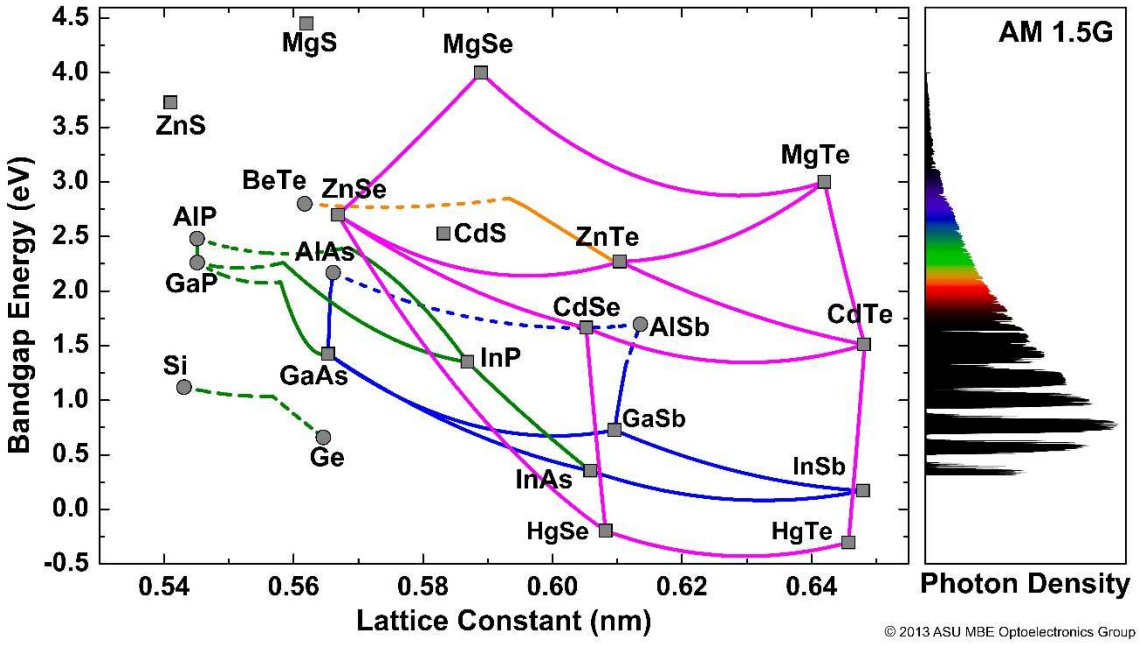

Fig. 4-6 Bandgap Energy vs. Lattice Constant for Some Group IV, III-V and II-VI Compound Semiconductors.

The MBE optoelectronics group at Arizona State University is the first group to grow CdTe/MgCdTe double-heterostructures (DHs) on InSb substrates [12]. The growth was carried out by a dual-chamber VG V80H MBE system with two separate III-V and II-VI growth chambers connected under ultra-high vacuum (UHV). Time-resolved photoluminescence measurements revealed a maximum carrier lifetime of 86 ns in the first set of monocrystalline MgCdTe/CdTe DH samples [12]. This value is an order of magnitude longer than the lifetime in polycrystalline CdTe [44]. The growth of MgCdTe/CdTe DHs on InSb substrates enjoys several advantages [45], including:

1. InSb substrates are cheaper than the CdTe substrates.
2. InSb substrates have lower defect density than CdTe substrates.

3. InSb (Eg = 0.17 eV) substrate is conductive. The resistance at the CdTe/InSb interface is negligible.
4. The oxide on the surface of the InSb substrates can be easily removed in the III-V growth chamber.
5. The wider-bandgap MgCdTe barrier layers confine the carriers in the CdTe active layer, reducing the surface recombination.

Further research have been conducted to improve the carrier lifetime in the CdTe/MgCdTe double-heterostructures (DHs), including increasing the Mg compositions and the thicknesses of the MgCdTe barrier layers [46][47][48], as well as incorporating Zn in the CdTe active layer to make it perfectly lattice-matched to InSb substrate [49]. The longest carrier lifetime observed in CdTe/MgCdTe DHs is 3.6 μs. These findings indicate that the non-radiative recombination inside of, and at the boundary of the CdTe absorber is significantly suppressed. CdTe can be easily doped n-type using Indium doping. In the moderately doped ($N_d \leq 10^{18}$ cm^{-3}) n-type CdTe samples, the Indium dopants are fully ionized at room temperature, and the carrier lifetimes are approaching the radiative limit [50].

In this chapter, we report the Photoluminescence Quantum Efficiency (PLQE) measurements on the n-type CdTe/MgCdTe DHs grown on InSb substrates. PLQE accounts for the luminescence emitting from the sample top surface to free space, and so it is also referred as External Luminescent Quantum Efficiency (η_{ext}) in the paper. The Internal Luminescent Quantum Efficiency (η_{int}) is calculated from the measured PLQE taking into account the structure of the sample and the absorption of the substrate. We find

that the recombination of photogenerated carriers is radiative recombination dominated in moderately doped n-type CdTe/MgCdTe DHs, with an implied V_{oc} over 1.1 V.

4.4 Photoluminescence Quantum Efficiency Measurement

The layer structure of the CdTe/MgCdTe DH samples is shown in Fig. 4-7. The 1-μm-thick CdTe absorber is sandwiched between two 15-nm-thick $Mg_{0.46}Cd_{0.54}Te$ barriers. Note that the 1-μm absorber thickness is chosen because it absorbs 98% of the above-bandgap-photons under the AM1.5G spectrum. The whole DH is doped with Indium, and a 30-nm-thick CdTe cap layer is used to protect the DH.

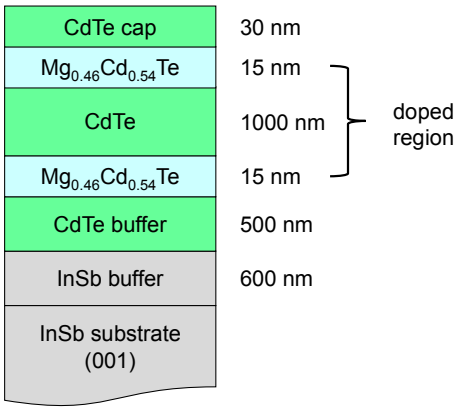

Fig. 4-7 Layer Structure of Indium-Doped CdTe/$Mg_{0.46}Cd_{0.54}Te$ Double-Heterostructures.

The PLQE measurement setup, as shown in Fig. 4-8, is similar to the setup adopted by I. Schnitzer, et al [51]. The η_{ext} is measured by comparing the PL of a CdTe/MgCdTe DH sample with the scattered light from a Spectralon Lambertian reflector. The excitation source is a 532 nm diode pumped solid state (DPSS) laser with a beam radius of 0.54±0.01 mm on the sample.

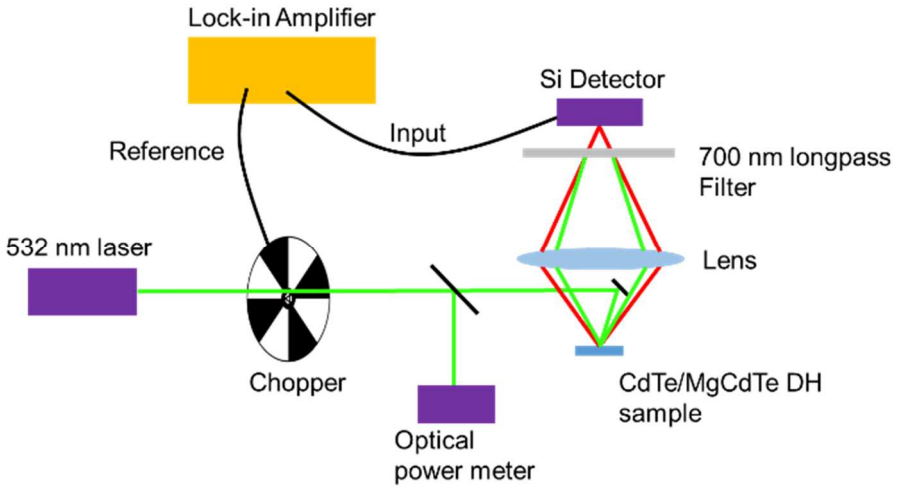

(a)

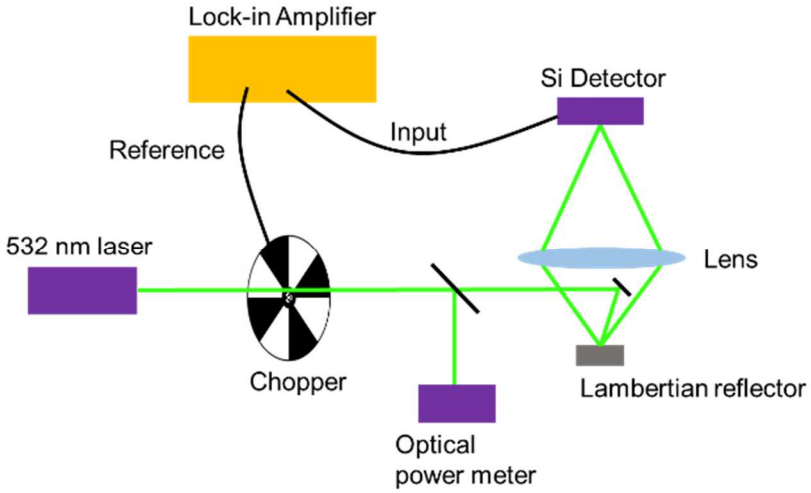

(b)

Fig. 4-8 Photoluminescence Quantum Efficiency (PLQE), or External Luminescence Quantum Efficiency (η_{ext}), Measurement System Setup. The PLQE of the CdTe/MgCdTe Double-Heterostructure (DH) Sample is Measured by Comparing (a) the Signal from the DH Sample, and (b) the Signal from a Lambertian Reflector.

As shown in Fig. 4-8 (a), when the laser shines on the Lambertian reflector, the reflector scatters the incident light into Lambertian distribution. A portion of the scattered

light is collected by the lens and measured by a Silicon detector as reference signal. The reference signal (S_{ref}) reading on the lock-in amplifier is:

$$S_{ref} = R_{ref}\phi_{laser}C_{laser} \tag{4.1}$$

where R_{ref} is the reflectance of the Lambertian reflector, ϕ_{laser} is the photon-flux of the excitation laser. C_{laser} is the throughput of the optical setup at the laser wavelength, which includes the contributions from the lens, and the responsivity of the photodetector.

As shown in Fig. 4-8(b), when the laser illuminates the PL sample, the sample emits PL with a peak wavelength of 820 nm. The angular distribution is also Lambertian. PL is collected by the lens and passes through a long-pass filter before entering the Si detector. The long-pass filter prevents the scattered laser light from entering the Si detector. The signal reading (S_{PL}) on the lock-in amplifier is:

$$S_{PL} = \phi_{PL}C_{PL} \tag{4.2}$$

where ϕ_{PL} is total photon-flux of the PL (ϕ_{PL}) from the sample. C_{PL} is the throughput of the optical setup at the PL, which includes the contributions from the lens, the longpass filter and the responsivity of the photodetector. The exact values of C_{laser} and C_{PL} do not need to be known. The ratio of C_{laser}/C_{PL} can be accurately estimated by considering the transmission curves of the lens and the longpass filter, and the responsivity of the photodetector at two wavelengths.

The total photon-flux of the PL (ϕ_{PL}) from the sample is:

$$\phi_{PL} = R_{ref}\phi_{laser}\frac{S_{PL}}{S_{ref}}\frac{C_{laser}}{C_{PL}} \tag{4.3}$$

The External Luminescent Quantum Efficiency (η_{ext}) is the ratio of the number of luminescent photons to the number of absorbed photons:

$$\eta_{ext} = \frac{\phi_{PL}}{A_{DH}\phi_{laser}} \tag{4.4}$$

where A_{DH} is the absorptance of the double-heterostructure at the laser wavelength. For the sample structure in Fig. 4-7, A_{DH} is 55% at the laser wavelength according to wave-optics calculations.

The η_{ext} as a function of excitation power density of five n-type CdTe/MgCdTe DH samples with different doping levels are shown in Fig. 4-9. The η_{ext} is almost constant as the power density varies from 20 to 200 mW/cm^2. Time resolved photoluminescence (TRPL) measurements have revealed a carrier lifetime of 110 ns in the sample doped at 1×10^{16} cm^{-3} [50]. Under 200 mW/cm^2 excitation, the excess carrier density is estimated to be 3×10^{14} cm^{-3}, much lower than the doping levels, which explains the relative independence of η_{ext} on the excitation power density.

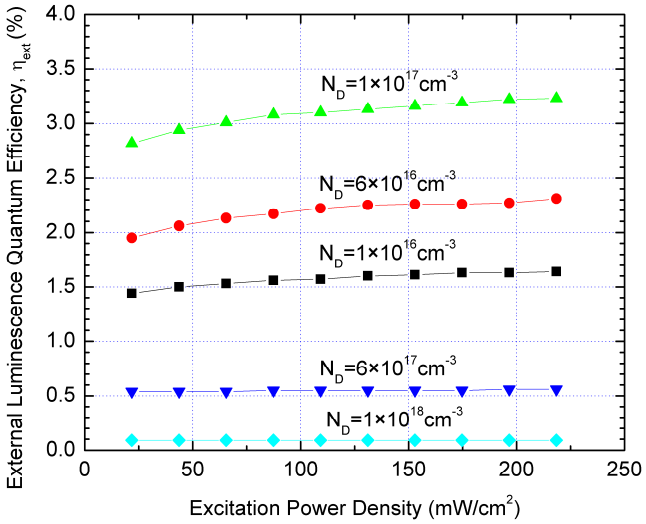

Fig. 4-9 External Luminescence Quantum Efficiency (η_{ext}) as a Function of the Excitation Power Density for Indium-Doped n-type Samples with Carrier Concentrations Ranging from 10^{16} cm^{-3} to 10^{18} cm^{-3}.

η_{ext} is related to the Internal Luminescent Quantum Efficiency (η_{int}) through [7]:

$$\eta_{ext} = \frac{\eta_{int}\gamma_e^f}{1-\eta_{int}\gamma_r} \tag{4.5}$$

where γ_e^f is the photon-extraction factor from the front surface, the probability of a luminescent photon to escape from the front surface to free space. γ_r is the photon-recycling factor, the probability of a luminescent photon to be reabsorbed in the absorber region. Using the method presented in [13], γ_e^f and γ_r are estimated to be 0.95±0.1% and 80±2%, respectively. It is worth noting that the γ_e^f and γ_r calculations are very sensitive to the absorber layer thickness and the absorption coefficient of CdTe near the band edge, which is difficult to be measured accurately, leading to the large error bar of these two

parameters. With these parameters, the relation between η_{ext} and η_{int} is shown in Fig. 4-10, along with the measured η_{ext} of CdTe/MgCdTe DHs at various doping levels.

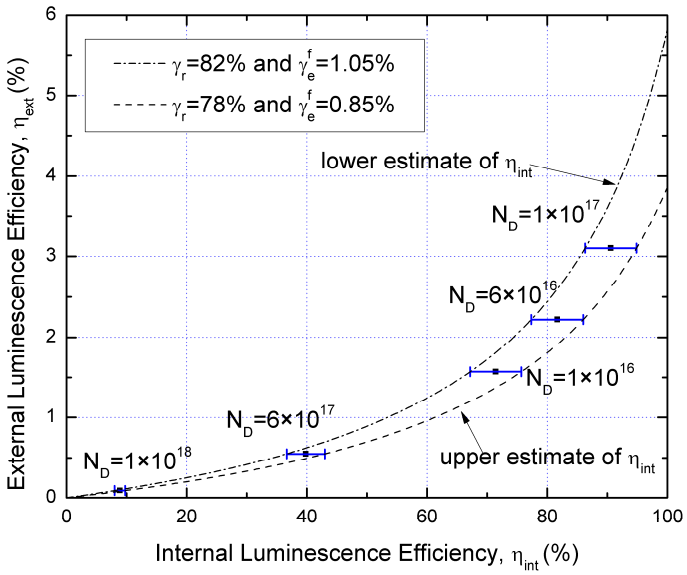

Fig. 4-10 External Luminescence Quantum Efficiency (η_{ext}) as a Function of Internal Luminescence Quantum Efficiency (η_{int}). The Lower Estimate of η_{int} is Shown in the Line with γ_r=82% and γ_e^f=1.05%; the Upper Estimate of η_{int} is the Line with γ_r=78% and γ_e^f=0.85%. The Measured η_{ext} and the Estimation of η_{int} of Five CdTe/MgCdTe DH Samples with Different Doping Levels are Also Shown.

The implied V_{oc} is calculated using the formula of [13][14][15][16][17]:

$$V_{oc} = V_{db} + \frac{kT}{q}\ln(\eta_{ext}) \tag{4.6}$$

where V_{db} is the detailed-balance open-circuit voltage, which is 1.22 V for 1-μm-thick CdTe solar cells.

The measurement results of five n-type CdTe/MgCdTe DH samples with different doping levels are summarized in Table 4-3. A maximum η_{ext} of 3.1% is observed from the

sample with a doping concentration of 10^{17} cm^{-3} at one-sun 100 mW/cm^2 power density. η_{ext} drops for lightly doped ($N_D \leq 6\times10^{16}$ cm^{-3}) and heavily doped ($N_D \geq 6\times10^{17}$ cm^{-3}) samples. The η_{ext} of 3.1% corresponds to η_{int}= 91±4%, i.e. about 91% of the carriers recombine radiatively in the absorber. The sample has a maximum implied V_{oc} of 1.13 V, which is approaching the theoretical limit of 1.17 V for CdTe solar cells with an absorbing substrate.

Table 4-3 Summary of Measurement Results

Sample Number	**A1712**	**A1695**	**A1707**	**A1694**	**A1699**
N_D (cm^{-3})	1×10^{16}	6×10^{16}	1×10^{17}	6×10^{17}	1×10^{18}
η_{ext} at one sun	1.6%	2.2%	3.1%	0.55%	0.09%
η_{int}	71±4%	82 ±4%	91±4%	40±3%	8.9±0.9%
Implied V_{oc} (V)	1.11	1.12	1.13	1.09	1.04

4.5 Summary of Chapter

The non-radiative recombination inside of, and the at the boundary of the CdTe absorber has been significantly reduced due to the MBE growth on lattice-matched InSb substrates, and the effective carrier confinement provided by the MgCdTe barrier layers. As a result, moderately doped ($N_D \approx 10^{17}$ cm^{-3}) n-type CdTe/MgCdTe DH samples become radiative recombination dominated. A maximum External Luminescent Quantum Efficiency of 3.1% is observed from a 1-μm-thick CdTe/MgCdTe DH doped to 10^{17} cm^{-3}, corresponding to an Internal Luminescence Quantum Efficiency (η_{int}) of 91±4 %, and an implied V_{oc} of 1.13 V, which is 0.37 V below the bandgap of CdTe. Due to its high quantum

yield, the CdTe/MgCdTe material system may find other applications in optoelectronics, such as lasers and light-emitting diodes.

CHAPTER 5

RECORD-EFFICIENCY MONOCRYSTALLINE CdTe/MgCdTe DOUBLE-HETEROSTRUCTURE SOLAR CELLS

5.1 Solar Cells without a PN Junction

It is commonly believed that a PN junction is necessary for a solar cell, and the electric filed at the PN junction is required to separate the photo-generated electrons and holes. This notion has been refuted by several researchers [52][53][54]. U. Würfel, et al. argued that the charge carrier separation in a solar cell is achieved by the differences in conductivities of electron and holes to the respective contacts [52]. PN junctions are carrier-selective by providing more holes in the p-type region, and more electrons in the n-type region.

In the 1970s, M. A. Green invented the metal-insulator-semiconductor (MIS) solar cell [53]. The semiconductor is passivated by a thin oxide layer. Minority carriers in the semiconductor absorber tunnel through the oxide layer to the metal contact. In 1985, E. Yablonovitch et al. [54] claimed that an ideal solar cell should be constructed in the form of a double-heterostructure. More importantly, the wide-bandgap contact layers do not need to be single-crystal and lattice-matched to the high quality absorber. The contact layer can be disordered and of poor quality, however the interface states at the heterojunction need to be passivated. Nowadays, almost all the record efficiency solar cells are constructed in the form of double-heterostructures, including epitaxial III-V [13], Silicon, and lead-halide perovskite solar cells.

The record efficiency silicon solar cell is HIT (heterojunction with intrinsic thin-layer) cell, which has achieved a record efficiency of 25.6% in 2014 [55]. In a HIT cell, the absorber is n-type c-Si wafer, passivated with intrinsic hydrogenated amorphous silicon (a-Si:H). The high-quality absorber generates the highest V_{oc} of 750 mV among all kinds of Silicon solar cells [56]. N-type and p-type a-Si:H layers act as electron and hole contacts. The contact layers can be defective without affecting the absorber quality and the voltage of the solar cells. An alternative passivation technique is an ultra-thin layer of Silicon Oxide (SiO_x). In the TOPCon (Tunnel Oxide Passivated Contact) cell [57], a monocrystalline Si absorber is passivated with an ultra-thin layer of tunnel oxide.

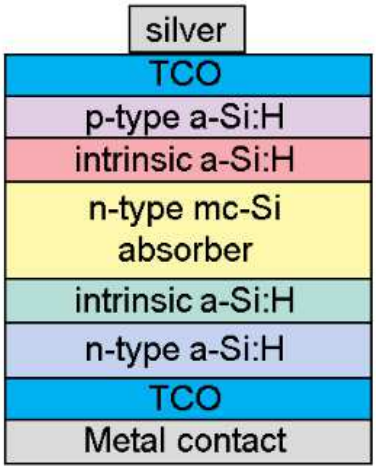

Fig. 5-1 Layer structure of Silicon-Heterojunction Solar Cell [56]. It Consists of a Double-Heterostructure: Narrow-Bandgap Monocrystalline Si Sandwiched between Wider-Bandgap Hydrogenated Amorphous Silicon (a-Si:H) Layers.

In 2013, planar heterojunction lead-halide perovskite solar cells [58] achieved an efficiency of over 15%. The cell is in the form of a p-i-n configuration; the lead-halide

perovskite ($CH_3NH_3PbI_{3-x}Cl_x$) absorber is sandwiched between electron and hole contact layers, made of TiO_2 and spiro-OMeTAD, respectively. A unique property of lead-halide perovskite is this material is very tolerant to defects and impurities, because the energy levels of the detect states fall near the band edges. Laser cooling is realized in polycrystalline lead-halide perovskite, which requires a high internal luminescence quantum efficiency (η_{int}) of ~99% [59]. The η_{int} is similar to the epitaxial grown GaAs [51], and thus, lead-halide perovskite is joining the top-league of optoelectronics [60].

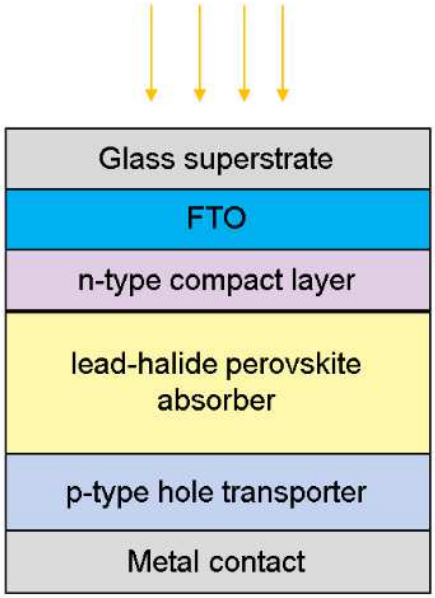

Fig. 5-2 Layer Structure of a Planar Heterojunction Lead-Halide Perovskite Solar Cell [58].

5.2 CdTe/MgCdTe DH Solar Cell with P-type a-Si:H Hole Contact

We applied the concept of carrier-selective contacts to make record-efficiency monocrystalline CdTe solar cells [61]. CdTe can be easily doped n-type, but is difficult to

be doped p-type. To solve this problem, we used an n-type CdTe absorber, and p-type a-Si:H for hole-extraction. The cell structure, shown in Fig. 5-3 (a), consists of an MBE grown CdTe/MgCdTe DH on an InSb substrate, a PECVD (Plasma-enhanced chemical vapor deposition) deposited p-type hydrogenated amorphous silicon (a-Si:H) contact layer, and an Indium Tin Oxide (ITO) top electrode. The CdTe absorber is sandwiched between lattice-matched MgCdTe barrier layers that confine carriers in the CdTe layer. Since the band alignment between CdTe and MgCdTe is Type-I, the i-MgCdTe layer introduces barriers for both electrons and holes. However, after putting the p-type a-Si:H contact layer on the top, the confinement of electrons and holes will be asymmetric. As shown in Fig. 5-3 (b), the hole contact layer induces band-bending in the CdTe absorber, thus the hole concentration is much higher than the electron concentration at the i-MgCdTe/n-CdTe interface. As a result, many more holes than electrons diffuse across the i-MgCdTe layer. The quasi-Fermi-level splitting is generated in the absorber, and the defective hole contact layer is outside of the absorber. So, it does not affect the voltage of the solar cell.

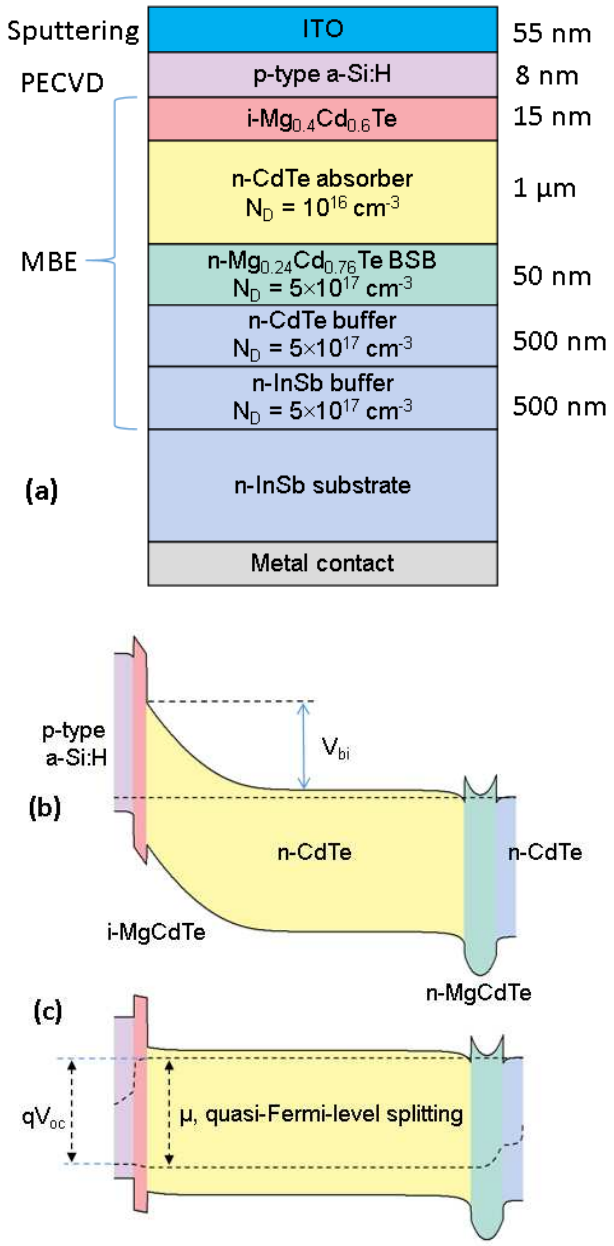

Fig. 5-3 (a) Layer Structure of the CdTe/MgCdTe Double-Heterostructure Solar Cell with a p-type a-Si:H as the Contact Layer and the Schematic Band Edge Diagram at (B) Equilibrium and (C) Open-Circuit.

The band-bending (or built-in voltage, V_{bi}) in the CdTe absorber is crucial for the selective transport of holes to the hole-contact layer. A forward bias voltage decreases the

band-bending and reduces the selectivity of the carrier transport to the hole contact, resulting in an increased number of electrons moving across the i-MgCdTe layer and recombining in the hole-contact layer. As illustrated in Fig. 5-3(c) the band diagram at open-circuit, due to the non-ideal band alignment between hole-contact material and n-CdTe, V_{oc} is lower than the quasi-fermi-level separation in the CdTe absorber. To determine V_{bi}, capacitance-voltage (CV) measurements are conducted after the deposition of p-type a-Si:H on the CdTe/MgCdTe DH, using a mercury probe with a contact area of 4.56×10^5 μm^2. Fig. 2 shows the measurement results. With a constant doping concentration, the capacitance is related to the applied reverse-bias voltage V through the formula of:

$$C = A\sqrt{\frac{qK_s\varepsilon_0 N_D}{2(V_{bi}+V)}} \tag{5.1}$$

where A is the area of the junction, $K_s\varepsilon_0$ is the dielectric constant of the semiconductor, and N_D is the donor concentration.

The built-in voltage, V_{bi}, is determined to be 1.1 V from the $1/C^2$-V plot, as shown in Fig. 5-4(a). V_{bi} is the intersection of $1/C^2$ on the x-axis. The doping concentration as a function of the depletion region width is shown in Fig. 5-4(b). The measured doping concentration is the same as the nominal value of 1×10^{16} cm^{-3} from 0.25 μm to 0.8 μm. The carrier concentration increases at the bottom of the absorber layer, which is beneficial to the electron transport across the n-MgCdTe back-side barrier layer.

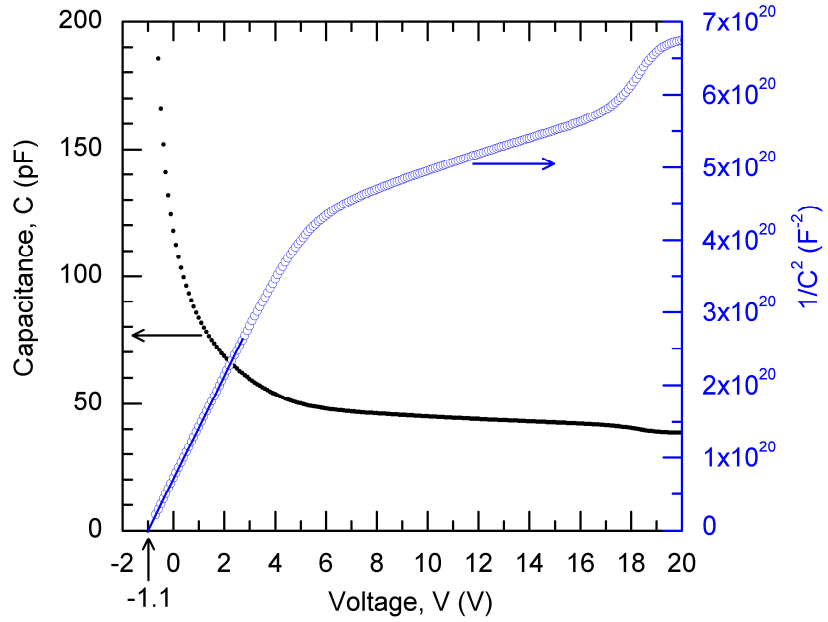

(a)

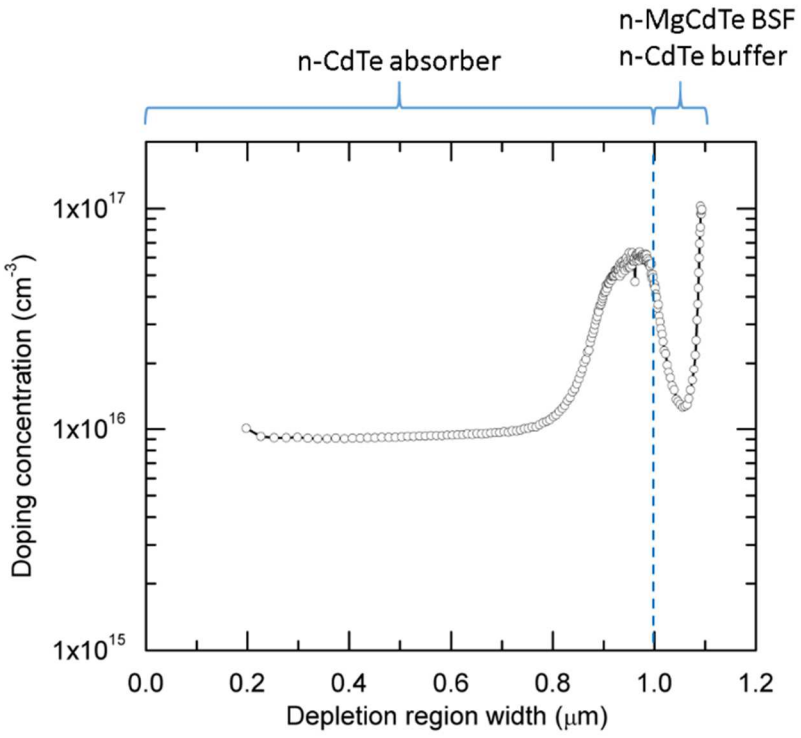

(b)

Fig. 5-4 (a) Capacitance-Voltage Measurement Results, and (b) the Measured Carrier Concentration in the CdTe/MgCdTe Double-Heterostructure.

5.3 Anderson's rule and the its assumptions

The band diagram shown in Fig. 5-3 (b) uses Anderson's rule [62]. This section discusses the Anderson's rule and its assumptions. B. KuhnHeinrich, et al. reported the MBE growth of CdTe/$Mg_xCd_{1-x}Te$ quantum wells (QWs) on $Cd_{0.96}Zn_{0.04}Te$ substrate [42]. Photoluminescence excitation (PLE) measurement was conducted at low temperature to determine the exciton binding energies in the QW and the band offset. The band alignment between CdTe and $Mg_xCd_{1-x}Te$ is type-I with a valence band-offset of 30%.

The band alignment between p-type amorphous silicon and CdTe can be theoretically estimated using the Anderson's rule. The Aderson's rule is based on the assumption that the vacuum levels of two materials that form a heterojunction should be continuous at the interface [62][63]. According to Anderson's rule, the conduction band offset at the heterojunction is determined by the difference in electron affinity:

$$\Delta E_c = \chi_1 - \chi_2 \tag{5.2}$$

where ΔE_c is the conduction band offset; and χ_1 and χ_2 are the electron affinity of the two materials forming the heterojunction.

For the p-type a-Si:H/CdTe heterojunction, the energy levels are shown in Fig. 5-5. The electron affinity of a-Si:H (χ_{a-Si}) is 3.9 eV according to Ref. [64]. The bandgap (Eg) of a-Si:H is ~1.7 eV [65]. According to Ref. [66], the electron affinity and bandgap of CdTe are 4.3 eV and 1.5 eV, respectively. Therefore, the conduction band offset (ΔE_c) between p-type a-Si:H and CdTe is 0.4 eV. The band-alignment between a-Si:H and CdTe is type-II, with valence band offset (ΔE_V) equal to 0.2 eV.

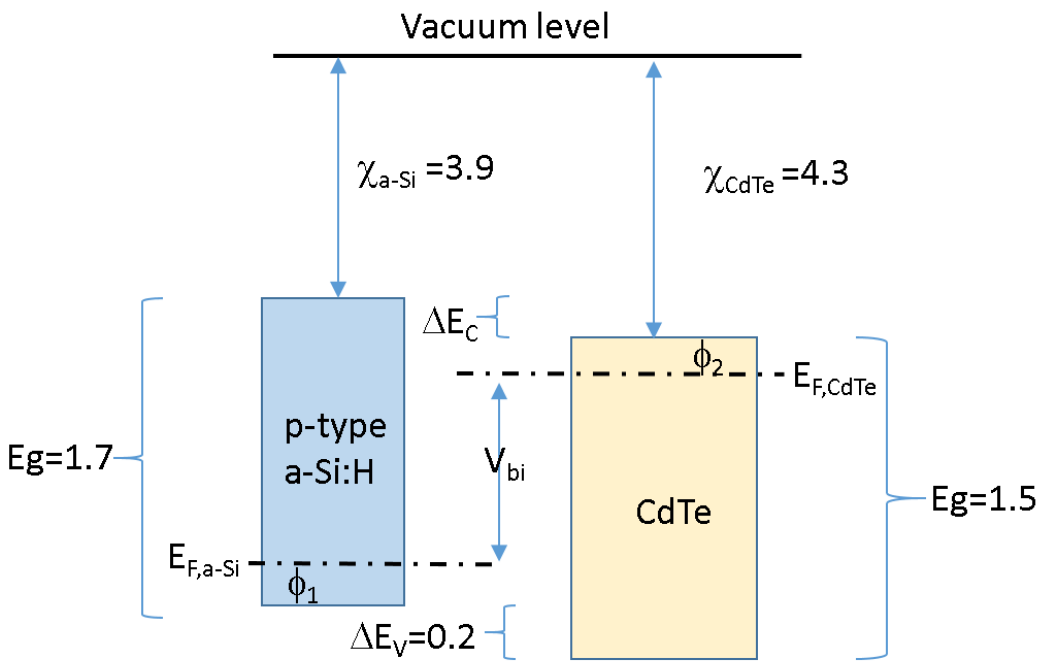

Fig. 5-5 Illustration of Electron Affinity, and Bandgap of P-type a-Si:H and CdTe.

The Fermi-levels of a-Si:H and n-type CdTe are different; a built-in voltage (V_{bi}) will be induced at the heterojunction, as shown in Fig. 5-6. The expression of V_{bi} is:

$$qV_{bi} = E_{g,CdTe} - \Delta E_V - \phi_1 - \phi_2 \tag{5.3}$$

where ϕ_1 is the distance of the Fermi-level to the valence band for p-type a-Si:H, and ϕ_2 is the distance of the Fermi-level to the conduction band for n-type CdTe. V_{bi} is about 1.1 V, if assuming ϕ_1 and ϕ_2 are both around 0.1 eV.

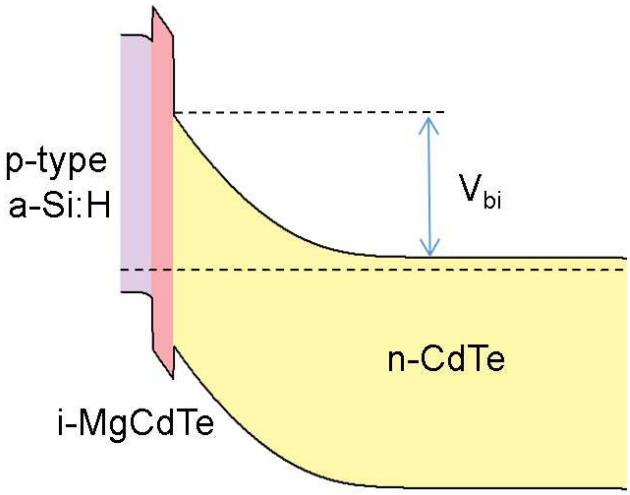

Fig. 5-6 Band-diagram of P-type a-Si:H, Intrinsic MgCdTe, and CdTe Heterojunction at Equilibrium.

The assumption of continuous vacuum level between the two materials at the heterojunction becomes invalid when there exist a large amount of interface charge [67]. The charge can originate from dangling bonds at the boundary of the bulk materials. Fig. 5-6 shows an example of heterojunction with interface dipole, and the corresponding band offset and the vacuum level, which is discontinuous at the heterojunction.

Experimental study, such as capacitance-voltage measurement, or X-ray photoelectron spectroscopy, can determine if there exists any interface dipole between p-type a-Si:H and CdTe.

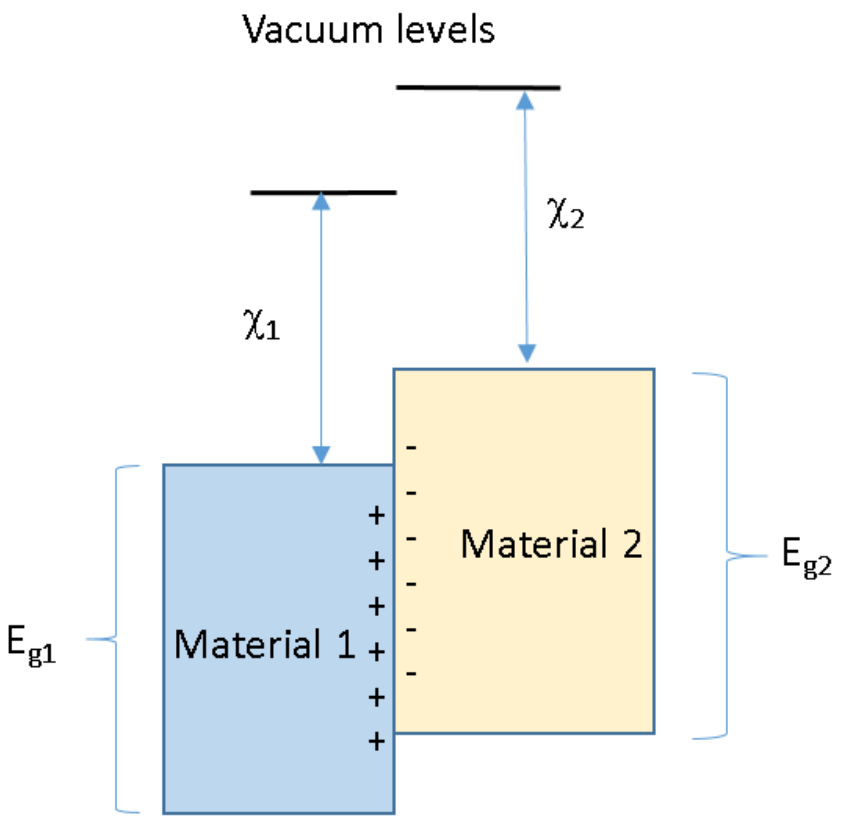

Fig. 5-7 Band Offset and Vacuum Levels When There Exists Interface Dipole at the Heterojunction.

5.4 Measurement Setup and Experimental Results

Fig. 5-8 shows the fabricated devices. P-type a-Si:H covers the entire sample. Round ITO patches with diameters of 1.5 mm, 2mm and 3 mm are deposited on top of the a-Si:H layer. The conductivity of the a-Si:H layer is low. The cell area is defined by the conductive ITO, which has a sheet resistance of 80 Ω/sq. The solar cell sample is placed on a gold-plated silicon carrier wafer. The IV-curves are measured using a 2-point-probe.

One probe tip touches the conductive gold-plated silicon carrier wafer. The other probe measures the IV-curves from the ITO patch.

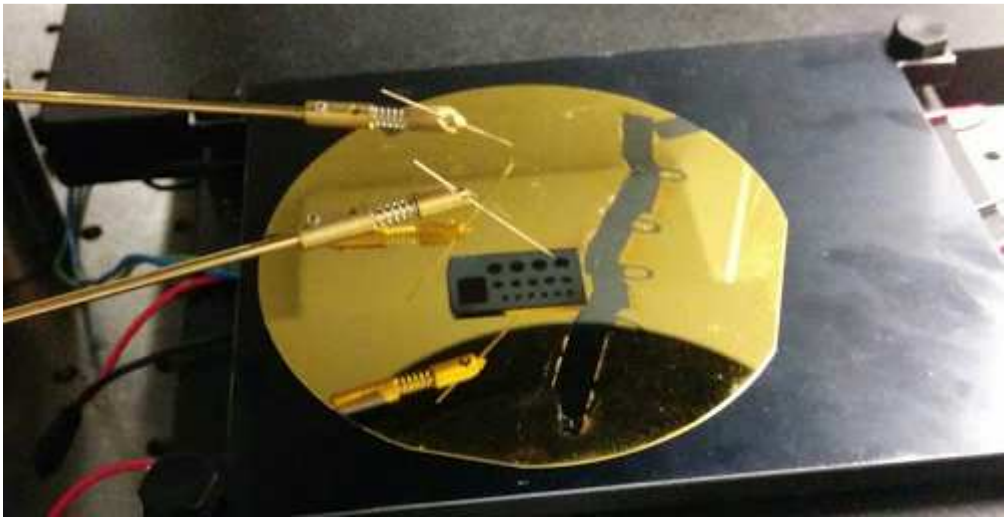

Fig. 5-8 Picture of the Monocrystalline Cdte/Mgcdte Double-Heterostructure Solar Cell and the Measurement Setup.

Fig. 5-9 shows the directly measured IV-curves. All the IV-curves exhibit V_{oc} greater than 1.1 V, with a maximum value of 1.122 V. However, there is a large variation in J_{sc}, ranging from 22 mA/cm^2 to 24 mA/cm^2. The reason is the ITO patches are deposited using a shadow mask. The edge of the ITO is not clearly defined, leading to the uncertainty in device areas and the J_{sc}.

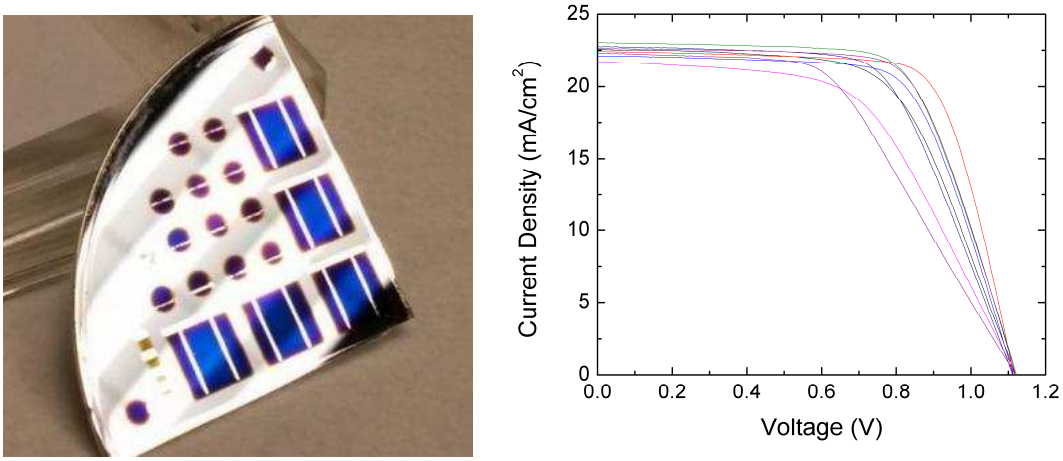

(a) (b)

Fig. 5-9 IV Measurement Results: (A) Picture of the Solar Cell Devices, and (B) Directly Measured IV-Curves from Selected Devices Fabricated on a Same Piece of Sample.

External Quantum Efficiency (EQE) measurements are conducted by shining a small monochromatic light beam on the ITO patch. We believe EQE measurement results are more accurate compared to direct IV measurements for small area devices, because the EQE measurement is independent of the cell area. To accurately determine J_{sc}, EQE measurements are conducted. By integrating the EQE curve, shown in Fig. 5-10 (a), times the AM1.5G spectrum, the current in the active area is $J_{sc} = 23.3$ mA/cm^2. Next, the directly measured IV-curve scaled so that it matches the EQE measurement result of $J_{sc} = 23.3$ mA/ cm^2, and the active area efficiency is calculated to be 18.8%.

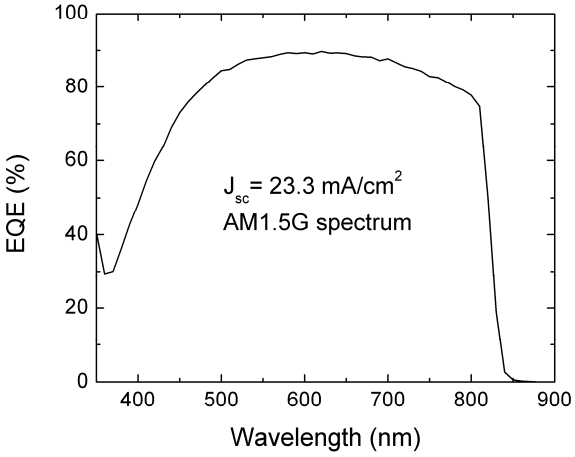

(a)

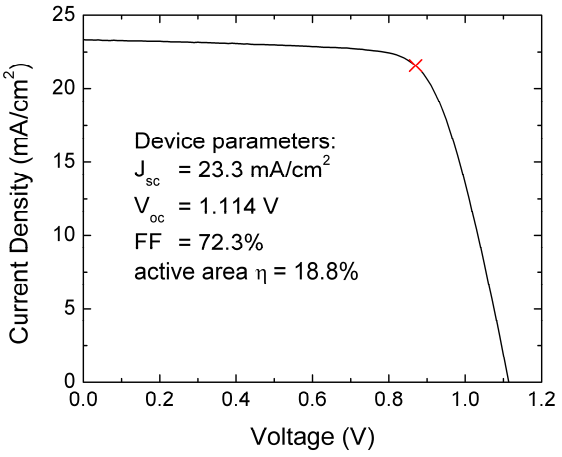

(b)

Fig. 5-10 (a) External Quantum Efficiency (EQE) Result and (B) the IV Curve of the Most Efficient Cell.

To analyze the loss mechanisms that reduce the photocurrent, the reflectance and absorptance spectrum of each layer is calculated using wave-optics, as shown in Fig. 5-11. The absorptance of the CdTe absorber layer resembles the measured EQE closely, indicating that the carrier collection efficiency in the solar cell is close to unity, which is expected since the minority carrier diffusion length in n-CdTe is estimated to be 5 μm,

much longer than the absorber thickness. Integrating the absorptance of the CdTe absorber with the AM1.5G spectrum gives a J_{sc} = 23 mA/cm^2. The losses of photocurrent due to reflectance and parasitic absorptions are also shown in Fig. 5-11. J_{sc} can be improved by employing double-layer antireflection coatings, wider-bandgap hole contact layers, and a thicker CdTe absorber.

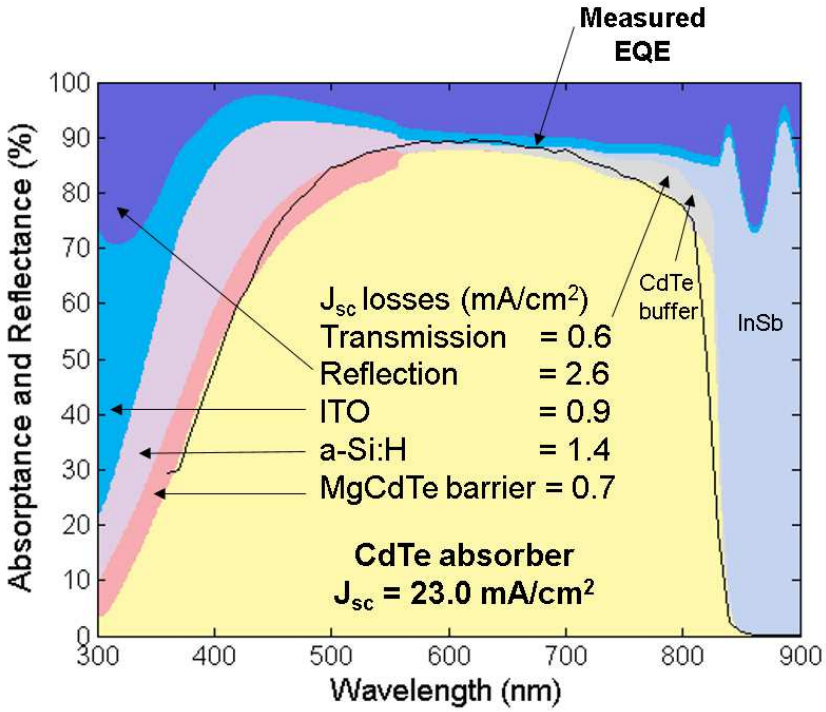

Fig. 5-11 Calculated Reflectance, Transmittance and Absorptance Spectra of a CdTe/MgCdTe DH Solar Cell with a Typical Device Structure Consisting of 55 nm ITO, 8 nm a-Si:H, 15 nm $Mg_{0.4}Cd_{0.6}Te$ Front Barrier, and 1 μm CdTe Absorber.

5.5 Possible Reasons for the Low Fill-Factor

The 72.3% FF of the CdTe/MgCdTe double-heterostructure solar cell is relatively low compared to record efficient solar cells. It may be attributable to the potential barrier for holes. The difference between the hole quasi-Fermi-level and the valence band edge of the i-MgCdTe front barrier layer is ϕ_h. The hole-concentration and the conductivity of holes in the i-MgCdTe layer are:

$$p = N_v \exp\left(-\frac{\phi_h}{kT}\right) \tag{5.4}$$

$$\sigma_h = q\mu_h p \tag{5.5}$$

Assuming ϕ_h = 0.6 eV, N_v = 1.4×10^{19} cm^{-3}, μ_h = 100 cm^2/(V·s), and a 20 nm i-MgCdTe layer thickness, the contact resistance for holes will be ~100 Ω·cm^2. This is a large series resistance. The contact resistance increases exponentially with ϕ_h. Note the relationship between V_{bi} and ϕ_h. A hole-contact material that induces a larger V_{bi} can significantly reduce the contact resistance, and may improve FF.

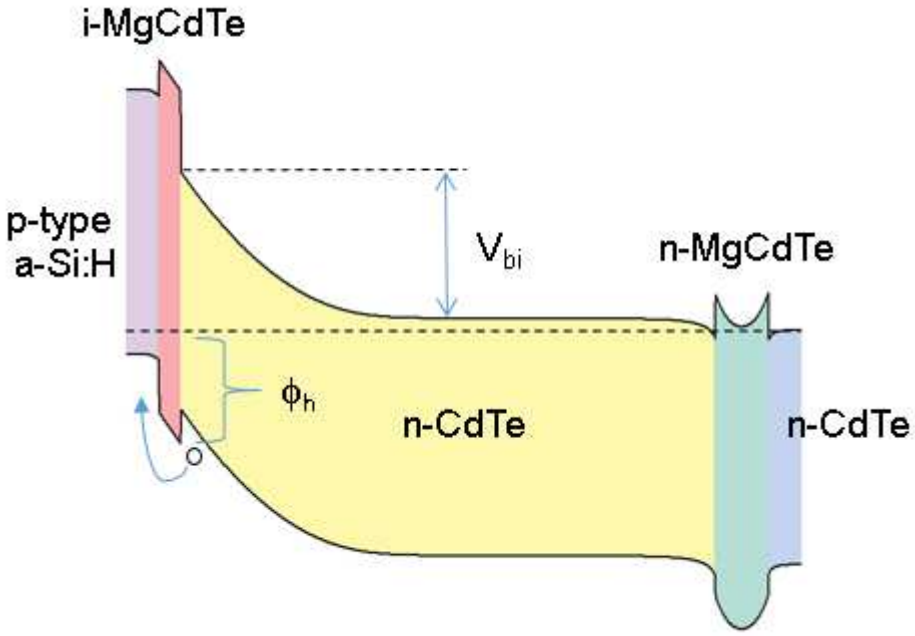

Fig. 5-12 Band-diagram at Equilibrium of Monocrystalline CdTe/MgCdTe Double-heterostructure Solar Cell with p-type a-Si:H Hole Contact Layer.

Transmission line measurements can experimentally measure the contact resistance and explore the reasons for the low FF. Fig. 5-13 shows a conceived test structure for the transmission line measurements. P-type a-Si:H induces band-bending in the n-type CdTe layer, and a p-type channel is formed near the top of the CdTe layer. If assuming the p-type channel is more conductive than the p-type a-Si:H and the i-MgCdTe layers, the current flow in the test structure will be shown as the red lines. The contact resistance from the metal contact to the CdTe layer can be extracted by measuring contact pads with difference spacing.

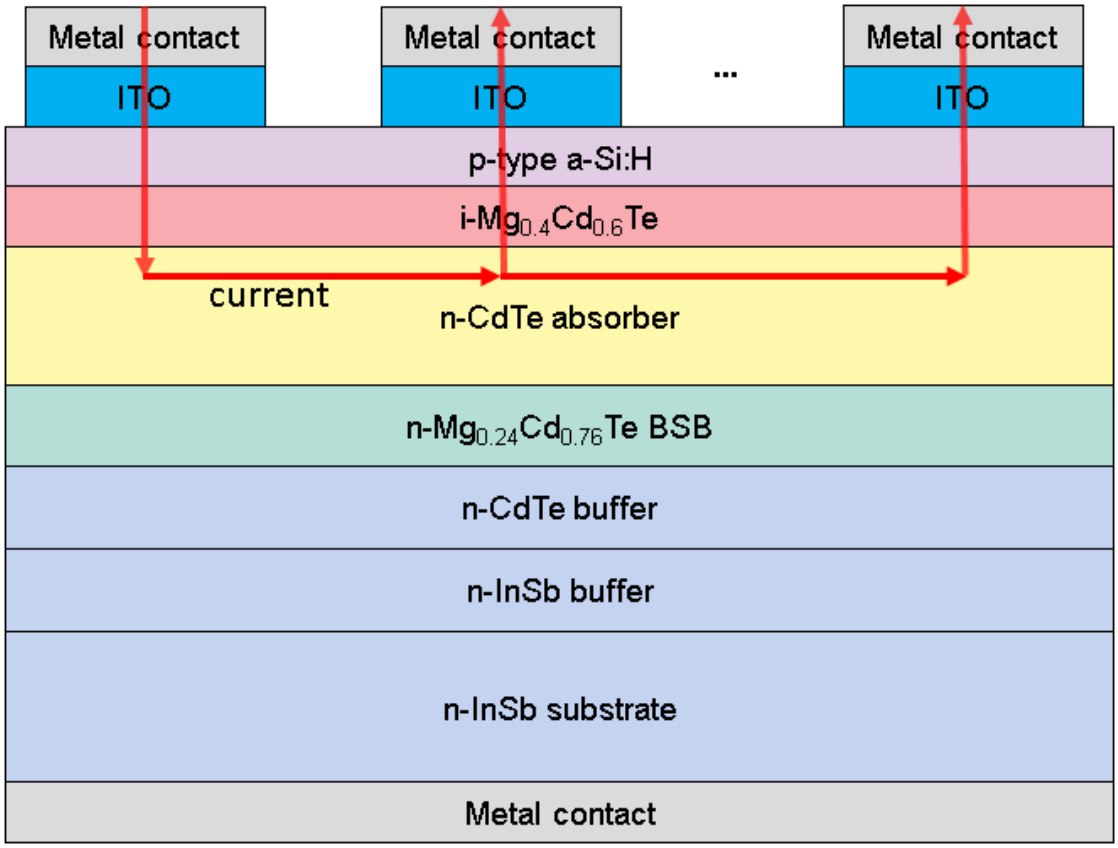

Fig. 5-13 A Test Structure for Transmission Line Measurements with Red Lines Showing the Direction of Current Flow.

Temperature-dependent light-IV measurements can reveal the physical mechanisms for the low FF. Fig. 5-14 shows the light-IV curves measured at difference cell temperatures from 20 °C to 120 °C. V_{oc} decreases from 1.085 V to 0.836 V, while FF increases from 52.2% to 59.1%. It is indicative that is a temperature dependent mechanism limits the FF.

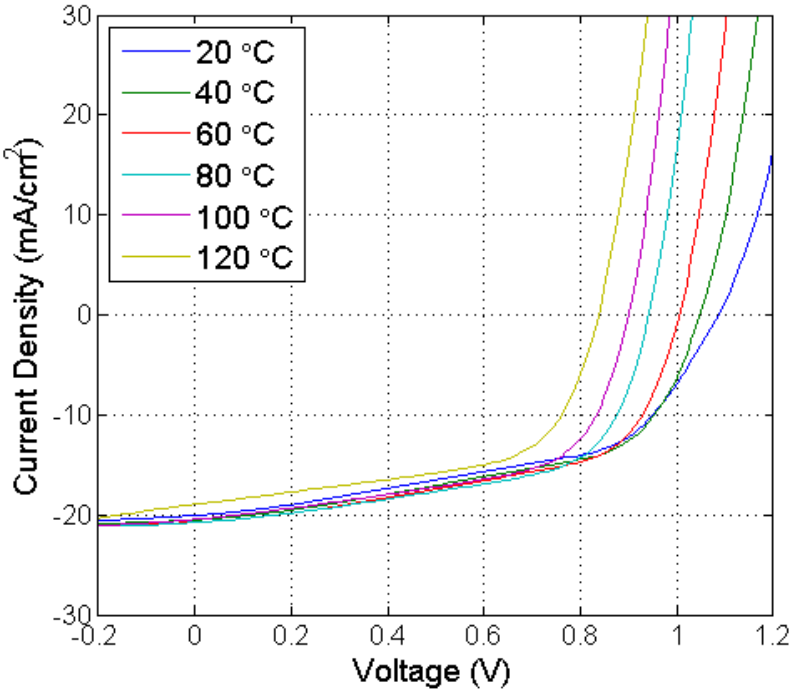

Fig. 5-14 Light-IV Measurements at Difference Cell Temperatures.

We assume that the FF is limited by R_s. Fig. 5-15 shows the equivalent circuit of a solar cell with series resistance (R_s). The IV relationship of the solar cells is:

$$J = J_{sc} - J_0 \exp\left(\frac{q(V - R_s J)}{kT}\right) \tag{5.6}$$

Since there is a one-to-one relationship between FF and R_s, R_s at each temperature can be estimated. R_s is estimated using the experimentally measured J_{sc}, V_{oc}, and FF. Fig. 5-16 shows R_s as a function of cell temperature. R_s decreases with temperature rapidly from 20 °C to 80 °C. At higher temperatures, the R_s reduction slows down, and seems to be saturating. There may exist temperature-dependent and temperature-independent mechanisms in the solar cell. At a higher temperature, holes are more energetic to diffuse across the i-MgCdTe front barrier. This may be the temperature-dependent R_s mechanisms.

Possible temperature-independent mechanisms include contact resistance at interfaces between layers as well as series resistance within each layer.

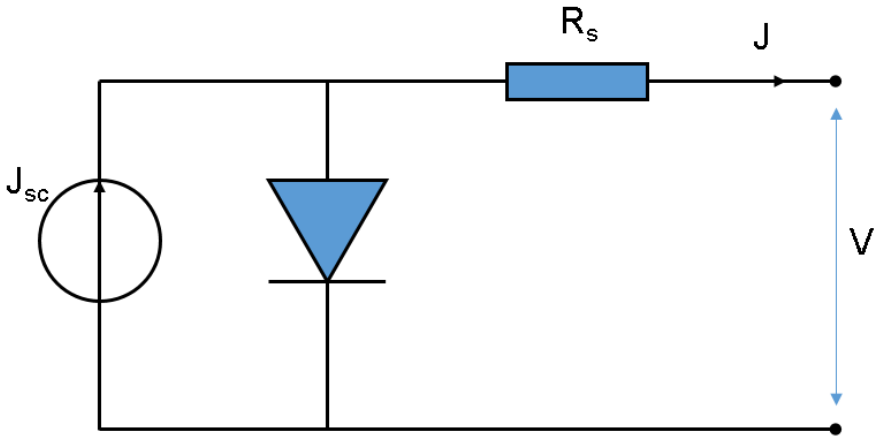

Fig. 5-15 Equivalent Circuit of a Solar Cell with Series Resistance (R_s).

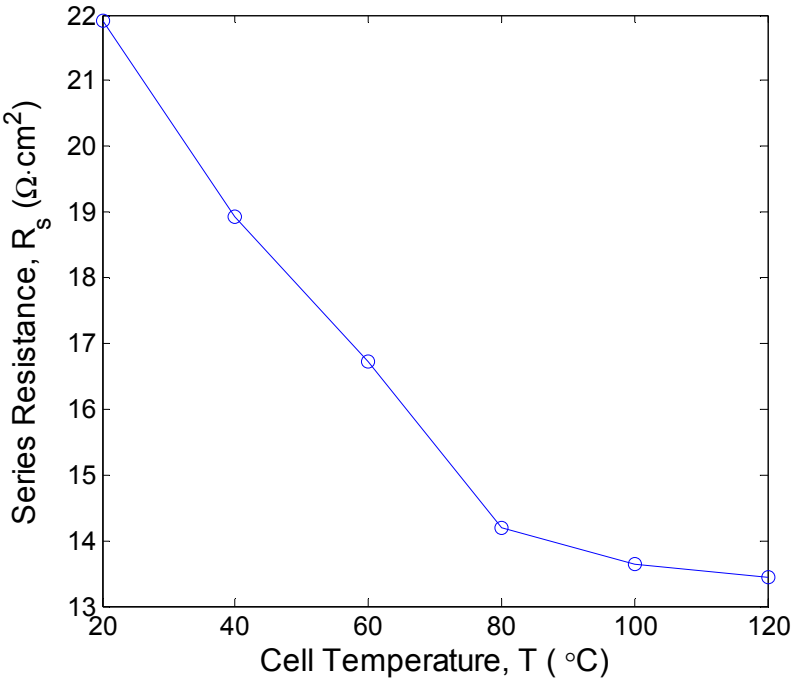

Fig. 5-16 Series Resistance as a Function of Cell Temperature.

5.6 Summary of Chapter

In summary, monocrystalline CdTe solar cells with 1-μm-thick absorber layers and p-type a-Si:H hole contact layers are experimentally demonstrated, achieving a maximum V_{oc} of 1.122 V and a new record monocrystalline CdTe cell efficiency of 18.8% (active area). This efficiency is still lower than the record efficiency (22.1%) for thin-film CdTe solar cells. Further efficiency improvement is expected by optimizing the layer structures, including using a hole contact material that gives optimum band-bending in contact with n-CdTe, using more transparent hole contact layers, double layer antireflection coatings, and optimized contact grids to improve the photo-current.

The record-efficiency thin-film CdTe solar cell has a short-circuit current density (J_{sc}) of 30.25 mA/cm^2 (> 95% of the theoretical value), and a decent fill-factor (FF) of 79.4%, however, the V_{oc} (only 876 mV) is far below the theoretical limit [39]. J_{sc} and FF are difficult to improve because they are approaching the theoretical limits. Future improvement of efficiency may rely on increasing V_{oc}. A unique feature of the monocrystalline CdTe/MgCdTe solar cell is the ultra-high V_{oc} over 1.1 V due to the effective passivation provided by the MgCdTe layer, and the high n-type doping level in CdTe. This result suggests that V_{oc} of thin-film CdTe solar cells may be improved by inserting MgCdTe thin layers between the CdS/CdTe and the CdTe/ZnTe interfaces, or using n-type CdTe absorbers. Fig. 5-17 shows the envisioned cell structure. This design will reduce the interface recombination and allow CdTe cells to be made much thinner than conventional thin-film CdTe solar cells, conserving the rare earth element of Tellurium. For the n-type CdTe absorber design shown in Fig. 5-17 (c), the PN junction is placed at

the rear. This design has proven to be superior to front-junction design for GaAs [13] and GaInP solar cells.

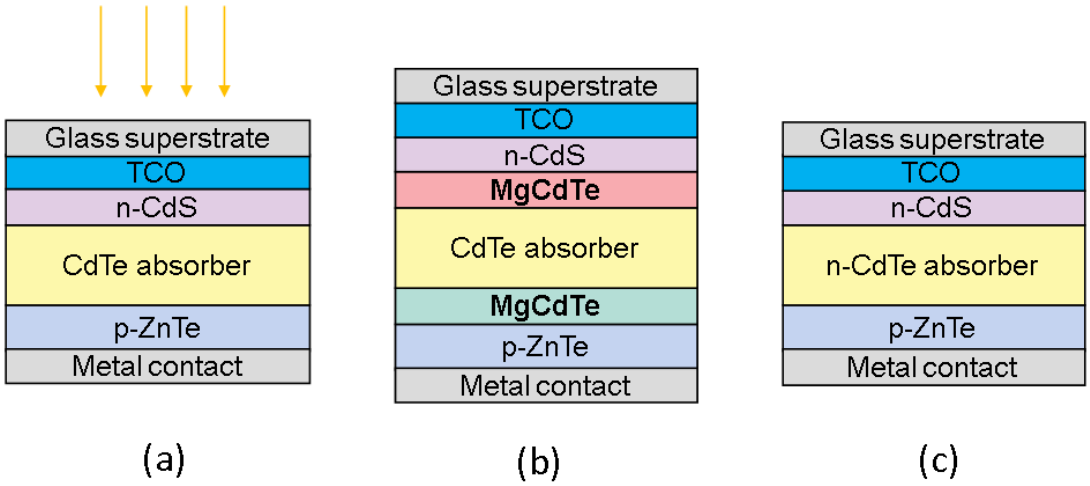

Fig. 5-17 Layer Structure of (a) State-of-the-Art Thin-Film CdTe Solar Cell; (b) the Envisioned Thin-Film CdTe Solar Cell with MgCdTe Passivation Layers, and (c) n-type CdTe Absorber.

CHAPTER 6

CONCLUSION AND OUTLOOK

6.1 Conclusion

The dissertation has developed a detailed-balance model for solar cells with finite absorber thicknesses and practical material parameters in Chapter 2. Given a cell structure, first, calculate the emittance/absorptance to every direction. Second, evaluate the short circuit current density (J_{sc}), and the dark current density (J_0) before obtaining the IV-curves and the efficiencies. The concepts of photon-recycling, photon-extraction, and external luminescence quantum efficiency were discussed. It is necessary to include photon-recycling effect in the simulation of solar cells approaching the radiative limit.

Chapter 3 studied the impact of below-bandgap-absorption (Urbach tail) on the limiting efficiency of solar cells. In general, the presence of an Urbach tail reduces the limiting efficiency of solar cells. Solar cells with non-zero below-bandgap absorption cannot beat the Shockley-Queisser limit, which is obtained when the absorptance spectrum is a step-function centered at the optimum bandgap.

Chapter 4 reviewed the status and challenges of thin-film CdTe solar cells. The efficiency of thin-film CdTe solar cells are limited by the low open-circuit voltage due to the large non-radiative recombination in the polycrystalline CdTe absorber and the low-level of p-type doping. The material quality of CdTe is significantly improved by epitaxial growth on lattice-matched InSb substrates and the use of MgCdTe passivation layers. The recombination processes in Indium-doped n-type CdTe/MgCdTe double-heterostructures are radiative recombination dominated. The maximum external luminescent quantum

efficiency (η_{ext}) is 3.1%, corresponding to an internal luminescent quantum efficiency (η_{int}) of 91%, and an implied V_{oc} of 1.13 V. The implied V_{oc} is extracted to actual voltage using a p-type hydrogenated amorphous silicon hole-contact layer, achieving V_{oc} over 1.1 V, and a maximum active area efficiency of 18.8% (J_{sc} = 23.3 mA/cm^2, V_{oc} = 1.114 V, and FF = 72.3%). Chapter 6 described the design of the solar cells and measurement results.

An solar cell structure is a photovoltaic absorber sandwiched between carrier-selective electron and hole contacts. Ideal, the absorber should have a bandgap close to the optimum value according to the Shockley-Queisser model, a negligible Urbach tail, and a high electron-to-photon conversion efficiency.

6.2 Future Work

Crystalline silicon is the most successfully commercialized photovoltaic technologies taking up 90% of the market share [68]. The record efficiency of 25.6% achieved in 2014 [55] is approaching its practical efficiency limit [69]; further efficiency improvement is more and more challenging. Achieving higher efficiencies is critical to lowering down the cost of electricity generated by photovoltaic (PV) systems, because cell encapsulation cost and balance of system (BOS) cost are the largest cost contributors [68] and these costs are proportional to the area of solar cell modules.

Dual-junction 1.1 eV/1.7 eV tandem cell has a theoretical limiting efficiency of 45% under one-sun AM1.5G spectrum [70]. Combining an efficient 1.7 eV bandgap top solar cell with silicon cell may further improve the cost-effectiveness of solar panels. However, only a handful of wide-bandgap PV absorbers have demonstrated a high enough efficiency

to provide efficiency gain in tandem-configuration, among them are GaInP [71] and lead halide perovskites [72][73]. Placing a 1.8 eV GaInP cell on top of a Silicon cell gives a combined efficiency of 29.8% [71], which is lower than the epitaxial grown dual-junction GaInP/GaAs thin-film solar cells whose efficiencies are over 31% [74]. The industry has proved that II-VI materials can be deposited on glass to make efficient thin-film cells. If the material quality of 1.7 eV thin-film absorbers made of (Mg, Zn)CdTe can be improved approaching radiative limit, they might become a cost-effective candidate for silicon-based tandem cells.

REFERENCES

[1] Steven Chu, and Arun Majumdar, "Opportunities and challenges for a sustainable energy future", *Nature*, Vol. 488, pp. 294 (2012)

[2] Sarah Kurtz, Harry Atwater, Angus Rockett, Tonio Buonassisi, Christiana Honsberg, and John Benner, "Solar research not finished", *Nature Photonics,* Vol. 10, pp. 141 (2016)

[3] William Shockley, and Hans J. Queisser, "Detailed balance limit of efficiency of pn junction solar cells", *Journal of Applied Physics*, Vol. 32, pp. 510 (1961)

[4] D. Ding, S. R. Johnson, S.-Q. Yu, S.-N. Wu, and Y.-H. Zhang, "A semi-analytical model for semiconductor solar cells", *Journal of Applied Physics*, Vol. 110, pp. 123104 (2011)

[5] Eli Yablonovitch, and George D. Cody, "Intensity enhancement in textured optical sheets for solar cells", *IEEE Transactions on Electron Devices*, Vol. ED-29, No. 2, pp. 300 (1982)

[6] A. Mart, J. L. Balenzategui, and R. F. Reyna, "Photon recycling and Shockley's diode equation", *Journal of Applied Physics*, Vol. 82, pp. 4067 (1997)

[7] J.-B. Wang, D. Ding, S. R. Johnson, S.-Q. Yu, and Y.-H. Zhang, "Determination and improvement of spontaneous emission quantum efficiency in GaAs/AlGaAs heterostructures grown by molecular beam epitaxy", *Physica Status Solidi (B)*, Vol. 244, No. 8, pp. 2740 (2007)

[8] W. van Roosbroeck, and W. Shockley, "Photon-radiative recombination of electrons and holes in germanium", *Physical Review*, Vol. 94, No. 6, pp. 1558 (1954)

[9] Donald A. Clugston, and Paul A. Basore, "PC1D version 5: 32-bit solar cell modeling on personal computers", in the proceedings of *IEEE 26th PVSC* (1997)

[10] S. M. Durbin, and J. L. Gray, "Numerical Modeling of Photon Recycling in Solar Cells", *IEEE Transactions on Electron Devices*, Vol. 41, No. 2, pp. 239 (1994)

[11] Sadao Adachi, *Optical constants of crystalline and amorphous semiconductors: numerical data and graphical information*, Kluwer Academic Publishers

[12] Michael J. DiNezza, Xin-Hao Zhao, Shi Liu, Alexander P. Kirk, and Yong-Hang Zhang, "Growth, steady-state, and time-resolved photoluminescence study of

CdTe/MgCdTe double heterostructures on InSb substrates using molecular beam epitaxy", *Applied Physics Letters*, Vol. 103, pp. 193901 (2013)

[13] M. A. Steiner, J. F. Geisz, I. García, D. J. Friedman, A. Duda, and S. R. Kurtz, "Optical enhancement of the open-circuit voltage in high quality GaAs solar cells", *Journal of Applied Physics*, Vol. 113, pp. 123109 (2013)

[14] Robert T. Ross, "Some Thermodynamics of Photochemical Systems", *Journal of Chemical Physics*, Vol. 46, pp. 4590 (1967)

[15] U. Rau, "Reciprocity relation between photovoltaic quantum efficiency and electroluminescent emission of solar cells", *Physical Review B*, Vol. 76, pp. 085303 (2007)

[16] Martin A. Green, "Radiative efficiency of state-of-the-art photovoltaic cells", *Progress in Photovoltaics: Research and Applications*, Vol. 20, pp. 472 (2012)

[17] Owen D. Miller, Eli Yablonovitch, and Sarah R. Kurtz, "Strong internal and external luminescence as solar cells approach the Shockley–Queisser limit", *IEEE Journal of Photovoltaics*, Vol. 2, No. 3, pp. 303 (2012)

[18] Weiquan Yang, Jacob Becker, Shi Liu, Ying-Shen Kuo, Jing-Jing Li, Barbara Landini, Ken Campman, and Yong-Hang Zhang, "Ultra-thin GaAs single-junction solar cells integrated with a reflective back scattering layer", *Journal of Applied Physics*, Vol. 115, pp. 203105 (2014)

[19] Jianhua Zhao, Aihua Wang, and Martin A. Green, "24.5% Efficiency Silicon PERT Cells on MCZ Substrates and 24.7% Efficiency PERL Cells on FZ Substrates", *Progress in Photovoltaics: Research and Applications*, Vol. 7, pp. 471 (1999)

[20] Stefaan De Wolf, Antoine Descoeudres, Zachary C. Holman, and Christophe Ballif, "High-efficiency Silicon heterojunction solar cells: A Review", *Green*, Vol.2, pp. 7 (2012)

[21] F. Urbach, "The long-wavelength edge of photographic sensitivity and of the electronic absorption of solids", *Physical Review*, Vol. 92, pp. 1324 (1953)

[22] John D. Dow, and David Redfield, "Toward a unified theory of Urbach's rule and exponential absorption edges", *Physical Review B*, Vol. 5, pp. 594 (1972)

[23] N. V. Kurik, "Urbach rule", *Physica Status Solidi (A)*, Vol. 8, pp. 9 (1971)

[24] C. H. Grein, and Sajeev John, "Temperature dependence of the Urbach optical absorption edge: A theory of multiple phonon absorption and emission sidebands", *Physical Review B*, Vol. 39, No. 2, pp. 1140 (1989)

[25] Hitoshi Sumi, and Yutaka Toyozawa, "Urbach-Martienseen rule and exciton trapped momentarily by lattice vibrations", *Journal of the Physical Society of Japan*, Vol. 31, pp. 342 (1971).

[26] S. R. Johnson, and T. Tiedje, "Temperature dependence of the Urbach edge in GaAs", *Journal of Applied Physics*, Vol. 78, pp. 5609 (1995)

[27] E. D. Palik, *Handbook of Optical Constants of Solids*, Academic, New York, 1985.

[28] E. Belas, Š. Uxa, R. Grill, P. Hlídek, L. Šedivý, and M. Bugár, "High temperature optical absorption edge of CdTe single crystal", *Journal of Applied Physics*, Vol. 116, pp. 103521 (2014)

[29] M. Beaudoin, A. J. G. DeVries, S. R. Johnson, H. Laman, and T. Tiedje, "Optical absorption edge of semi-insulating GaAs and InP at high temperatures", *Applied Physics Letters,* Vol. 70, pp. 354 (1997)

[30] S. S. Ou, O. M. Stafsudd, and B. M. Basol, "Optical properties of electrochemically deposited CdTe films*", Journal of Applied Physics,* Vol. 55, pp. 3769 (1984)

[31] Yuan-Sheng Tyan, "Topics on thin film CdS/CdTe solar cells", *Solar Cells*, Vol. 23, pp. 19 (1988)

[32] Brian E. McCandless, and James R. Sites, "Cadmium Telluride Solar Cells", Chapter 14 of *Handbook of Photovoltaic Science and Engineering*, John Wiley & Sons (2003)

[33] J. Britt, and C. Ferekides, "Thin-film CdS/CdTe solar cell with 15.8% efficiency", *Applied Physics Letters*, Vol. 62, pp. 2851 (1993)

[34] S. A. Ringel, A. W. Smith, M. H. MacDougal, and A. Rohatgi, "The effects of $CdCl_2$ on the electronic properties of molecular-beam epitaxially grown CdTe/CdS heterojunction solar cells", *Journal of Applied Physics*, Vol. 70, pp. 881 (1991)

[35] X. Wu, R.G. Dhere, D.S. Albin, T.A. Gessert, C. DeHart, J.C. Keane, A. Duda, T.J. Coutts, S. Asher, D.H. Levi, H.R. Moutinho, Y. Yan, T. Moriarty, S. Johnston, K. Emery, and P. Sheldon, "High-Efficiency CTO/ZTO/CdS/CdTe Polycrystalline Thin-Film Solar Cells", *NCPV Program Review Meeting*, 14-17 October 2001

[36] http://investor.firstsolar.com/releasedetail.cfm?releaseid=956479

[37] Nicholas Strevel, Lou Trippel, Chad Kotarba, and Imran Khan, "Improvements in CdTe module reliability and long-term degradation through advances in construction and device innovation", *Photovoltaics International*, Vol. 22, pp. 1 (2013)

[38] Colin A. Wolden, Ali Abbasc, Jiaojiao Lib, David R. Diercksb, Daniel M. Meysinga, d, Timothy R. Ohnoe, Joseph D. Beache, Teresa M. Barnesd, and John M. Wallsc, "The roles of ZnTe buffer layers on CdTe solar cell performance", *Solar Energy Materials & Solar Cells*, Vol. 147, pp. 203 (2016)

[39] M. Gloeckler, I. Sankin, and Z. Zhao, "CdTe solar cells at the threshold to 20% efficiency", *IEEE Journal of Photovoltaics*, Vol. 3, No. 4, pp. 1389 (2013)

[40] J. M. Burst, J. N. Duenow, D. S. Albin, E. Colegrove, M. O. Reese, J. A. Aguiar, C.-S. Jiang, M. K. Patel, M. M. Al-Jassim, D. Kuciauskas, S. Swain, T. Ablekim, K. G. Lynn, and W. K. Metzger, "CdTe solar cells with open-circuit voltage breaking the 1V barrier", *Nature Energy*, 16015 (2016)

[41] A. Waag, H. Heinke, S. Scholl, C.R. Becker, and G. Landwehr, "Growth of MgTe and $Cd_{1-x}Mg_xTe$ thin films by molecular beam epitaxy", *Journal of Crystal Growth*, Vol. 131, pp. 607 (1993)

[42] B. Kuhn-Heinrich, W. Ossau, H. Heinke, F. Fischer, T. Litz, A. Waag, and G. Landwehr, "Optical investigation of confinement and strain effects in CdTe/(CdMg)Te quantum wells", *Applied Physics Letters*, Vol. 63, pp. 2932 (1993)

[43] R. F. C. Farrow, G. R. Jones, G. M. Williams, and I. M. Young, "Molecular beam epitaxial growth of high structural perfection, heteroepitaxial CdTe films on InSb (001)", *Applied Physics Letters*, Vol. 39, pp. 954 (1981)

[44] Darius Kuciauskas, Ana Kanevce, James M. Burst, Joel N. Duenow, Ramesh Dhere, David S. Albin, Dean H. Levi, and Richard K. Ahrenkiel, "Minority Carrier Lifetime Analysis in the Bulk of Thin-Film Absorbers Using Subbandgap (Two-Photon) Excitation", *IEEE Journal of Photovoltaics*, Vol. 3, No. 4, pp. 1319 (2013)

[45] Michael. J. DiNezza, "Monocrystalline ZnTe/CdTe/MgCdTe Double Heterostructure Solar Cells Grown on InSb Substrates by Molecular Beam Epitaxy", Doctoral dissertation (2014)

[46] Xin-Hao Zhao, Michael J. DiNezza, Shi Liu, Calli M. Campbell, Yuan Zhao, and Yong-Hang Zhang, "Determination of CdTe bulk carrier lifetime and interface recombination velocity of CdTe/MgCdTe double heterostructures grown by molecular beam epitaxy", *Applied Physics Letters*, Vol. 105, pp. 252101 (2014)

[47] Xin-Hao Zhao, Michael J. DiNezza, Shi Liu, Calli M. Campbell, Yuan Zhao, and Yong-Hang Zhang, "Time-resolved and excitation-dependent photoluminescence study of CdTe/MgCdTe double heterostructures grown by molecular beam epitaxy", *Journal of Vacuum Science & Technology B*, Vol. 32, pp. 040601 (2014)

[48] Shi Liu, Xin-Hao Zhao, Calli M. Campbell, Maxwell B. Lassise, Yuan Zhao, and Yong-Hang Zhang, "Carrier lifetimes and interface recombination velocities in CdTe/$Mg_xCd_{1-x}Te$ double heterostructures with different Mg compositions grown by molecular beam epitaxy", *Applied Physics Letters*, Vol. 107, pp. 041120 (2015)

[49] Shi Liu, Xin-Hao Zhao, Calli Campbell, Michael J. DiNezza, Yuan Zhao, and Yong-Hang Zhang, "Minority carrier lifetime of lattice-matched CdZnTe alloy grown on InSb substrates using molecular beam epitaxy", *Journal of Vacuum Science & Technology B*, Vol. 33, pp. 011207 (2015)

[50] Xin-Hao Zhao, Shi Liu, Yuan Zhao, Calli M. Campbell, Maxwell B. Lassise, Ying-Shen Kuo, and Yong-Hang Zhang, "Electrical and optical properties of n-type Indium-doped CdTe/$Mg_{0.46}Cd_{0.54}Te$ double heterostructures", *IEEE Journal of Photovoltaics*, Vol. 6, No. 2, pp. 552 (2016)

[51] I. Schnitzer, E. Yablonovitch, C. Caneau, and T. J. Gmitter, "Ultrahigh spontaneous emission quantum efficiency, 99.7% internally and 72% externally, from AlGaAs/GaAs/AlGaAs double heterostructures", *Applied Physics Letters*, Vol. 62, pp. 131 (1993)

[52] Uli Würfel, Andres Cuevas, and Peter Würfel, "Charge Carrier Separation in Solar Cells", *IEEE Journal of Photovoltaics*, Vol. 5, No. 1, pp. 461 (2015)

[53] M. A. Green, F.D. King, and J. Shewchun, "Minority carrier MIS tunnel diodes and their application to electron- and photo-voltaic energy conversion--I. Theory", *Solid-State Electronics*, Vol. 17, pp. 551 (1974)

[54] E. Yablonovitch, T. Gmitter, R. M. Swanson, and Y. H. Kwark, "A 720 mV open circuit voltage SiO_x:c-Si:SiO_x double heterostructure solar cell", *Applied Physics Letters*, Vol. 47, pp. 1211 (1985)

[55] Keiichiro Masuko, Masato Shigematsu, Taiki Hashiguchi, Daisuke Fujishima, Motohide Kai, Naoki Yoshimura, Tsutomu Yamaguchi, Yoshinari Ichihashi,

Takahiro Mishima, Naoteru Matsubara, Tsutomu Yamanishi, Tsuyoshi Takahama, Mikio Taguchi, Eiji Maruyama, and Shingo Okamoto, "Achievement of More Than 25% Conversion Efficiency With Crystalline Silicon Heterojunction Solar Cell", *IEEE Journal of Photovoltaics,* Vol. 4, No. 6, pp. 1433 (2014)

[56] Mikio Taguchi, Ayumu Yano, Satoshi Tohoda, Kenta Matsuyama, Yuya Nakamura, Takeshi Nishiwaki, Kazunori Fujita, and Eiji Maruyama, "24.7% Record Efficiency HIT Solar Cell on Thin Silicon Wafer", *IEEE Journal of Photovoltaics,* Vol. 4, No. 1, pp. 96 (2014)

[57] Frank Feldmann, Maik Simon, Martin Bivour, Christian Reichel, Martin Hermle, and Stefan W. Glunz, "Efficient carrier-selective p- and n-contacts for Si solar cells", *Solar Energy Materials & Solar Cells*, Vol. 131, pp. 100 (2014)

[58] Mingzhen Liu, Michael B. Johnston, and Henry J. Snaith, "Efficient planar heterojunction perovskite solar cells by vapour deposition", *Nature*, Vol. 501, pp. 395 (2013)

[59] Son-Tung Ha, Chao Shen, Jun Zhang, and Qihua Xiong, "Laser cooling of organic–inorganic lead halide perovskites", Nature Photonics, Vol 10, pp. 115 (2016)

[60] Eli Yablonovitch, "Lead halides join the top optoelectronic league", *Science*, Vol. 351, pp. 1401 (2016)

[61] Yuan Zhao, Mathieu Boccard, Shi Liu, Jacob Becker, Xin-Hao Zhao, Calli M. Campbell, Ernesto Suarez, Maxwell B. Lassise, Zachary Holman, and Yong-Hang Zhang, "Monocrystalline CdTe solar cells with open-circuit voltage over 1V and efficiency of 17%", *Nature Energy*, 16067 (2016)

[62] R. L. Anderson, "Germanium-Gallium Arsenide Heterojunctions", *IBM Journal of Research and Development*, Vol. 4, pp. 283, (1960)

[63] Edward T. Yu, James O. McCaldin, Thomas C. McGill, "Band Offset In Semiconductor Heterojunctions", *Solid State Physics*, Vol. 46, Academic Press (1992)

[64] Hideharu Matsuura, Tetsuhiro Okuno, Hideyo Okushi, and Kazunobu Tanaka, "Electrical properties of n-amorphouslp-crystalline silicon heterojunctions", *Journal of Applied Physics*, Vol. 55, pp. 1012 (1984)

[65] G.D. Cody, C.R. Wronski, B. Abeles, R.B. Stephens, B. Brooks, "Optical characterization of amorphous silicon hydride films", *Solar Cells*, Vol. 2, pp. 227 (1980)

[66] Sadao Adach, "Properties of Semiconductor Alloys: Group-IV, III–V and II–VI Semiconductors", John Wiley & Sons (2009)

[67] J. Tersoff, "Theory of semiconductor heterojunctions: The role of quantum dipoles", *Physical Review B*, Vol. 30, pp. 4874 (1984)

[68] Martin A. Green, "Commercial progress and challenges for photovoltaics", *Nature Energy*, 15015 (2016)

[69] David D. Smith, Peter Cousins, Staffan Westerberg, Russelle De Jesus-Tabajonda, Gerly Aniero, and Yu-Chen Shen, "Toward the practical limits of silicon solar cells," *IEEE Journal of Photovoltaics*, Vol. 4, pp. 1465 (2014)

[70] C. H. Henry, "Limiting efficiencies of ideal single and multiple energy gap terrestrial solar cells", *Journal of Applied Physics*, Vol. 51, pp. 4494 (1980).

[71] Stephanie Essig, Myles A. Steiner, Christophe Allebe, John F. Geisz, Bertrand Paviet-Salomon, Scott Ward, ´ Antoine Descoeudres, Vincenzo LaSalvia, Loris Barraud, Nicolas Badel, Antonin Faes, Jacques Levrat, Matthieu Despeisse, Christophe Ballif, Paul Stradins, and David L. Young, "Realization of GaInP/Si dual-junction solar cells with 29.8% 1-sun efficiency", *IEEE Journal of Photovoltaics*, Vol. 6, pp. 1012 (2016).

[72] Jérémie Werner, Ching-Hsun Weng, Arnaud Walter, Luc Fesquet, Johannes Peter Seif, Stefaan De Wolf, Bjoern Niesen, and Christophe Ballif, "Efficient monolithic perovskite/silicon tandem solar cell with cell area >1 cm^2", *Journal of Physical Chemistry Letters*, Vol. 7, pp. 161 (2016).

[73] Carolin M. Sutter-Fella, Yanbo Li, Matin Amani, Joel W. AgerIII, Francesca M. Toma, Eli Yablonovitch, Ian D. Sharp, and Ali Javey, "High photoluminescence quantum yield in band gap tunable bromide containing mixed halide perovskites", *Nano Letters*, Vol. 16, pp. 800 (2016).

[74] Myles A. Steiner, John F. Geisz, Ivan Garcia, Daniel J. Friedman, Anna Duda, Waldo J. Olavarria, Michelle Young, Darius Kuciauskas, and Sarah R. Kurtz, "Effects of Internal Luminescence and Internal Optics on V_{oc} and J_{sc} of III–V Solar Cells", *IEEE Journal of Photovoltaics*, Vol. 3, pp. 1437 (2013)